Journal of Computational and Applied Mechanics, Vol. 18, No. 1, (2023), pp. 35–84
DOI: 10.32973/jcam.2023.002

APPLICATION OF THE p-VERSION OF FEM TO HIERARCHIC ROD MODELS WITH REFERENCE TO MECHANICAL CONTACT PROBLEMS

István Páczelt
Institute of Applied Mechanics, University of Miskolc
3515 Miskolc-Egyetemváros, Hungary
Istvan.Paczelt@uni-miskolc.hu

Barna Szabó
Washington University in St. Louis, USA
barna.szabo@esrd.com

Attila Baksa
Institute of Applied Mechanics, University of Miskolc
3515 Miskolc-Egyetemváros, Hungary
Attila.Baksa@uni-miskolc.hu

[Received: February 22, 2023; Accepted: May 15, 2023]

Abstract. The formulation of a system of hierarchic models for the simulation of the mechanical response of slender elastic bodies, such as elastic rods, is considered. The present work is concerned with aspects of implementation and numerical examples. We use a finite element formulation based on the principle of minimum potential energy. The displacement fields are represented by the product of one-dimensional field functions and two-dimensional director functions. The field functions are approximated by the p-version of the finite element method. Our objective is to control both the model form errors and the errors of discretization with a view toward the development of advanced engineering applications equipped with autonomous error control procedures. We present numerical examples that illustrate the performance characteristics of the algorithm.

Mathematical Subject Classification: 74505, 74M15, 74K10
Keywords: error estimation, dimensional reduction, hierarchic rod models, p-version of finite element, mechanical contact

1. Introduction

There is growing interest in the democratization of recurrent numerical simulation tasks. Democratization aims to make software tools of numerical simulation easily and broadly accessible. We argue that making data generated by numerical simulation broadly accessible makes sense only if information about its quality and reliability are provided in a form understandable by persons whose expertise is not in numerical simulation. The advantages of democratization include productivity, consistency and compatibility with simulation process and data management (SPDM) systems. On the other hand, implementation without appropriate safeguards and error control can lead to errors that may not be detected in the early phases of design.

The idea of democratization is not new. Engineering handbooks and design manuals are examples of democratization practiced in the pre-computer age. Experts solved a variety of problems in mechanics by classical methods in parametric form. Those solutions were collected and made available to engineers through handbooks.

The classical approach to democratization had a serious limitation, however: Only highly simplified problems can be solved by classical methods. Therefore the handbook entries were not the problems engineers actually needed to solve. To get a rough estimate of the quantities of interest, engineers had to find handbook entries that were close in some sense to their problem on hand. The errors were primarily model form errors, that is, errors coming from simplifications in geometry and boundary conditions.

With the maturing of numerical simulation technology it is now possible to remove the limitations of classical engineering handbooks and provide parametric solutions for the problems that engineers actually need to solve. This is the main goal of democratization. The exceptionally rare talents of engineer-scientists who had populated conventional handbooks have to be democratized, that is, mapped into the world of modern-day analysts. Other important objectives are the accumulation and preservation of corporate knowledge and increased productivity.

The types of problems that are well suited for democratization have the following characteristics: The parameter space is small, the goals of computation are clearly defined and the number of times the problems have to be solved is sufficiently large to justify the investment of creating a dedicated application.

Questions relating to the level of confidence in the accuracy of the numerical solution have to be addressed by the expert analysts who create dedicated applications. When a mathematical problem is solved by a numerical method, commonly the finite element method, then it is necessary to provide information on how large the error in the quantity of interest (QoI) is. Without such an estimate the answer is incomplete. In many cases model form error is dominant. Ideally, the model form errors and the errors of approximation are equal. Applications must be designed so as to estimate and control both types of error.

In this paper the formulation of a system of hierarchic models is considered for the simulation of the mechanical response of slender elastic bodies, such as elastic rods. The displacement fields are represented by the product of one -dimensional field functions and two-dimensional director functions in the following functional form:

$$\mathbf{u} = \mathbf{u}(x, y, s) = \sum_{m=1}^{M} \mathbf{U}_{(m)}(x, y)\, \mathbf{h}^{(m)}(s)\,, \tag{1}$$

where $\mathbf{h}^{(m)}(s)$ are the field functions of the centerline coordinate s and $\mathbf{U}_{(m)}(x, y)$ are fixed director functions of the orthogonal coordinates in the direction of the normal and binormal to the centerline, respectively. In the case of homogeneous bars the director functions are polynomials (see, for example, Szabó and Babuška [1]. In the case of bars made of laminated composites, the director functions are piecewise polynomials (Actis [2]).

The field functions usually are Lagrange or Legendre polynomials, or more recently use of B-splines and isogeometric functional has also been discussed [3, 4].

The essential features of hierarchic models are: (a) The exact solutions corresponding to a hierarchic sequence of models converge in energy norm to the exact solution of the corresponding problem of elasticity, and (b) the exact solution of each model converges in energy norm to the same limit as the exact solution of the corresponding problem of elasticity with respect to the diameter of the cross section approaching zero.

A comprehensive overview of the theory of curved bars was presented by Antmann in [5]. As evidenced by Antmann's paper, the mathematical theory of curved bars is highly developed. We are concerned here with aspects of implementation and applications to problems of engineering interest.

The formulation of hierarchic models follows the same pattern as the formulation of three-dimensional models of continuum mechanics cast in variational form. Here we will consider the displacement formulation. Since the director functions are fixed, it is possible to integrate in the plane defined by the normal and binormal to obtain a set of one-dimensional field functions $\mathbf{h}^{(m)}(s),\ m = 1, \ldots, M$. This process is called dimensional reduction or semi-discretization.

In order to satisfy the condition that the exact solution of each model must converge in energy norm to the same limit as the exact solution of the corresponding problem of elasticity with respect to the diameter of the cross section approaching zero, it is necessary to make certain adjustments in the formulation for the low-order models. The Timoshenko beam model is an example of such adjustments (for a discussion of this point see Szabó and Babuška [1]).

Without any claim to completeness, we mention some important papers on dimensionally reduction in models in the following.

There are many papers on straight or curved beams [6–14], [15], plates [16–18] and shells [19–21], subjected to static loading as well as undergoing free vibration [22–24]. Varying material properties were examined in [25, 26], rods including piezo elements in [27], rod structures exposed to thermal effects in [28], and geometrically nonlinear cases in [29–31]. Solutions of contact problems are found for hierarchical beams in the case of elastic material in [32] and in the case of elastic-plastic deformation in [33].

In [34], we find analyses of hierarchical models for plates and shells covering static and eigenvalue problems. The paper addresses the question of whether models based on Kirchhoff's hypothesis are members of the hierarchic family. The effects of the boundary layer were also investigated. The complex nature of this topic is evidenced by the hundreds of references in the article.

Our primary goal is to present numerical results that highlight the main features of hierarchic models. We examine prismatic and plane-curved rods and rods with a spiral centerline, assuming that the material is homogeneous, isotropic, linearly elastic, the load is quasi-static, and the displacements and deformations are small, i.e., boundary value problems are solved within the framework of linear elasticity theory.

The three-dimensional reference solutions were obtained using the StressCheck finite element program [35] and Abaqus program [36]. In either case error control procedures were applied to ensure that the numerical errors are negligibly small.

We pay special attention to formulating the contact problem for beams and solving it effectively. We construct a solution in which class C problems defined in [1, 37] are reduced to class B problems using a positioning technique [38, 39] whereby the boundaries of the contact regions are also element boundaries.

Few works can be found in the literature related to the p-version finite element modeling of contact problems, even in the case of small displacements and deformations: References [40, 41] examine smooth problems, an axisymmetric friction problem is solved in [42] and a 3D spatial contact problem is solved using splines in [43]. Examples of wear calculations can be found in [44]. Frictionless and frictional contact of spatial supports at large displacements are addressed in [45–48]. Examples of hierarchical modeling are presented in [49]. Parts of the structure are modeled as 3D, 2D, 1D finite elements, using special transition elements.

This paper is organized as follows: The formulation of hierarchical models is described in Section 2. The problem of frictionless contact is formulated in Section 3. Examples, highlighting various aspects of dimensionally reduced hierarchic models, are presented in Section 4. In order to simplify the discussion, details are presented in the Appendices.

2. Formulation

2.1. **Model in the local curvilinear coordinate system.** We examine a linearly elastic body with a helical centerline of pitch H wound on a cylindrical surface of radius R_o as shown in Figure 1. The position vector of the centerline is:

$$\mathbf{r} = \mathbf{r}(\bar{\varphi}) = R_0 \left(\cos(\bar{\varphi})\,\mathbf{i} + \sin(\bar{\varphi})\,\mathbf{j}\right) + \frac{H}{2\pi}\bar{\varphi}\,\mathbf{k}, \tag{2}$$

where $\bar{\varphi}$ is the angle coordinate of the cylindrical coordinate system and s is the arc coordinate of the centerline. Using the Serret–Frenet reference frame [25], the normal, binormal and tangent unit vectors $(\mathbf{n}, \mathbf{b}, \mathbf{t})$ of the local coordinate system, the curvature κ, and the twist per unit length τ are obtained. The $\mathbf{n}$, $\mathbf{b}$ axes are the principal axes of the cross section. The notation is indicated in Figure 1.

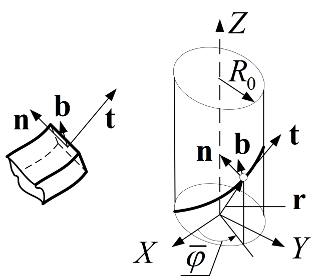

Figure 1. Centerline and unit vectors of the local coordinate system

2.2. **Displacements.** The displacement of an arbitrary point P of the body in the local curvilinear local coordinate system is given by (see Figure 2)

$$\mathbf{u} = \mathbf{u}(x, y, s) = u_n\mathbf{n} + u_b\mathbf{b} + u_t\mathbf{t} \equiv u_1\mathbf{e}_1 + u_2\mathbf{e}_2 + u_3\mathbf{e}_3\,, \tag{3}$$

where

$$\mathbf{u} = \mathbf{u}(x, y, s) = \sum_{m=1}^{M} \bar{\mathbf{h}}^{(m)}(x, y, s) = \sum_{m=1}^{M} \mathbf{U}_{(m)}(x, y)\ \mathbf{h}^{(m)}(s) \tag{4}$$

is the functional form of our approximation. The definition of

$$\bar{\mathbf{h}}^{(m)}(x, y, s)$$

depends on the choice of the hierarchic model. The function

$$\mathbf{U}_{(m)}(x, y)$$

represents the director functions. For example, letting $M = 3$, for homogeneous isotropic material we have

$$\bar{\mathbf{h}}^{(1)}(x, y, s) = \begin{bmatrix} u_{01} - y\,\chi_3 \\ u_{02} + x\,\chi_3 \\ u_{03} + y\,\chi_1 \ - x\,\chi_2 \end{bmatrix} + \begin{bmatrix} xu_{1x} \\ yu_{2y} \\ 0 \end{bmatrix} = \bar{\mathbf{h}}^{(1)0} + \bar{\mathbf{h}}^{(1)1} =$$

$$= \mathbf{U}_{(1),0}(x, y)\mathbf{h}^{(1)0}(s) + \mathbf{U}_{(1),1}(x, y)\mathbf{h}^{(1)1}(s) = \mathbf{U}_{(1)}(x, y)\mathbf{h}^{(1)}(s)\,, \tag{5a}$$

$$\bar{\mathbf{h}}^{(2)}(x, y, s) = \begin{bmatrix} (x^2\,u_{1x^2} + xy\,u_{1xy} + y^2 u_{1y^2}) \\ (x^2\,u_{2x^2} + xy\,u_{2xy} + y^2\,u_{2y^2}) \\ (x^2\,u_{3x^2} + xy\,u_{3xy} + y^2\,u_{3y^2}) \end{bmatrix} = \mathbf{U}_{(2)}(x, y)\mathbf{h}^{(2)}(s)\,, \tag{5b}$$

$$\bar{\mathbf{h}}^{(3)}(x, y, s) = \begin{bmatrix} (u_{1x^3}x^3 + u_{1x^2y}x^2y + u_{1xy^2}xy^2 + u_{1y^3}y^3) \\ (u_{2x^3}x^3 + u_{2x^2y}x^2y + u_{2xy^2}xy^2 + u_{2y^3}y^3) \\ (u_{3x^3}x^3 + u_{3x^2y}x^2y + u_{3xy^2}xy^2 + u_{3y^3}y^3) \end{bmatrix} = \mathbf{U}_{(3)}(x, y)\mathbf{h}^{(3)}(s)\,. \tag{5c}$$

Furthermore

$$\mathbf{U}_{(1),0} = \begin{bmatrix} 1 & 0 & 0 & 0 & 0 & -y \\ 0 & 1 & 0 & 0 & 0 & x \\ 0 & 0 & 1 & y & -x & 0 \end{bmatrix}, \ \mathbf{U}_{(1),1} = \begin{bmatrix} x & 0 \\ 0 & y \\ 0 & 0 \end{bmatrix},$$

$$\mathbf{U}_{(1)} = \begin{bmatrix} 1 & 0 & 0 & 0 & 0 & -y & x & 0 \\ 0 & 1 & 0 & 0 & 0 & x & 0 & y \\ 0 & 0 & 1 & y & -x & 0 & 0 & 0 \end{bmatrix}, \tag{6a}$$

$$\mathbf{U}_{(2)} = \begin{bmatrix} x^2 & xy & y^2 & 0 & 0 & 0 & 0 & 0 & 0 \\ 0 & 0 & 0 & x^2 & xy & y^2 & 0 & 0 & 0 \\ 0 & 0 & 0 & 0 & 0 & 0 & x^2 & xy & y^2 \end{bmatrix}, \tag{6b}$$

$$\mathbf{U}_{(3)} = \begin{bmatrix} x^3 & x^2y & xy^2 & y^3 & 0 & 0 & 0 & 0 & 0 & 0 & 0 & 0 \\ 0 & 0 & 0 & 0 & x^3 & x^2y & xy^2 & y^3 & 0 & 0 & 0 & 0 \\ 0 & 0 & 0 & 0 & 0 & 0 & 0 & 0 & x^3 & x^2y & xy^2 & y^3 \end{bmatrix}, \tag{6c}$$

where $u_{1x}, u_{2y};\ u_{0i},\ \chi_i;\ u_{ix^2}\,,\ u_{ixy},\ u_{iy^2};\ u_{ix^3}, u_{ix^2y}, u_{ixy^2}, u_{iy^3}\ i = 1, 2, 3$ are the one-dimensional field functions of s, the monomials $1,\ x,\ y;\ x^2,\ xy,\ y^2\,; x^3, x^2y, xy^2, y^3$ are the director functions. In the classical theory of beams only the linear terms

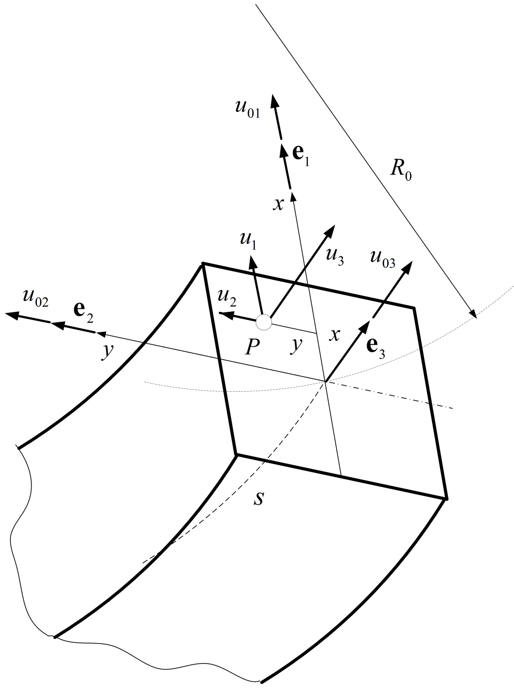

Figure 2. Notation: x, y, s – local coordinate system, $\mathbf{e}_1, \mathbf{e}_2, \mathbf{e}_3$ are the unit vectors, u_{01}, u_{02}, u_{03} are displacements of the center line, u_1, u_2, u_3 are displacements at an arbitrary point P, R_0 is the radius of cylinder

are retained. This is justified when the diameter of the cross section approaches zero. However, in practical problems one has to consider bars that have cross sections of finite diameters, in which case the higher-order terms may play an important role, depending on the goals of computation. As M increases, the solution of the fully three-dimensional problems is approximated progressively better in the norm of the formulation, in our case the energy norm, and the types of boundary conditions that can be applied increase. The director functions $\mathbf{U}_{(m)}(x, y)$ are polynomials constructed from the monomials of Pascal's triangle (see Appendix A).

2.3. **Deformations.** The deformation tensor at small deformation

$$\boldsymbol{\varepsilon} = \boldsymbol{\varepsilon}(x, y, s) = \frac{1}{2}(\mathbf{u} \otimes \nabla + \nabla \otimes \mathbf{u}) \tag{7}$$

can be calculated through a geometric equation. Here $\otimes$ denotes dyadic multiplication. The nabla operator is:

$$\nabla = \frac{\partial}{\partial x}\mathbf{e}_1 + \frac{\partial}{\partial y}\mathbf{e}_2 + \frac{R_1}{R_1 - x}\frac{\partial}{\partial s}\mathbf{e}_3 \equiv \frac{\partial}{\partial x}\mathbf{n} + \frac{\partial}{\partial y}\mathbf{b} + \frac{R_1}{R_1 - x}\frac{\partial}{\partial s}\mathbf{t} \tag{8}$$

, where $R_1 = 1/\kappa$ is the radius of curvature.

The axial and shear strains can be calculated as follows in the adopted curvilinear coordinate system:

$$
\begin{gathered}
\varepsilon_1=\frac{\partial u_1}{\partial x},\quad \varepsilon_2=\frac{\partial u_2}{\partial y},\quad \varepsilon_3=\frac{R_1}{R_1-x}\left(\frac{\partial u_3}{\partial s}-\frac{u_1}{R_1}\right),\\
\gamma_{12}=\frac{\partial u_1}{\partial y}+\frac{\partial u_2}{\partial x},\quad \gamma_{13}=\frac{R_1}{R_1-x}\left(\frac{\partial u_1}{\partial s}-\tau\, u_2+\kappa u_3\right)+\frac{\partial u_3}{\partial x},\\
\gamma_{23}=\frac{R_1}{R_1-x}\left(\frac{\partial u_2}{\partial s}+\tau u_1\right)+\frac{\partial u_3}{\partial y}.
\end{gathered}
\tag{9}
$$

It is seen from these relationships that some of the deformations depend only on the function itself and its x, y derivative, while others depend on the derivative with respect to s. We will introduce the following vectors using notation $(...)' = \partial(...)/\partial s$:

For Model 0:

$$
\begin{aligned}
&\mathbf{h}^{(1)0T}=[u_{01}\ u_{02}\ u_{03}\ \chi_1\ \chi_2\ \chi_3]\,,\quad \mathbf{h}^{(1)0\,'T}=[u'_{01}\ u'_{02}\ u'_{03}\ \chi'_1\ \chi'_2\ \chi'_3]\\
&\tilde{\boldsymbol{\psi}}_0^T=\tilde{\boldsymbol{\psi}}_0^T(s)=\left[\mathbf{h}^{(1)0T}\ \mathbf{h}^{(1)0\,'T}\right]=\\
&\qquad=[u_{01}\ u_{02}\ u_{03}\ \ \chi_1\ \chi_2\ \chi_3\ \ u'_{01}\ u'_{02}\ u'_{03}\ \ \chi'_1\ \chi'_2\ \ \chi'_3]\,.
\end{aligned}
\tag{10}
$$

For Model 1:

$$
\begin{gathered}
\mathbf{h}^{(1)T}=\left[\mathbf{h}^{(1)0T}\ \mathbf{h}^{(1)1T}\right],\quad \mathbf{h}^{(1)1T}=[u_{1x},\ u_{2y}]\,,\quad \mathbf{h}^{(1)1\,'T}=\left[u'_{1x},\ u'_{2y}\right],\\
\tilde{\boldsymbol{\psi}}_1^T=\tilde{\boldsymbol{\psi}}_1^T(s)=\left[\tilde{\boldsymbol{\psi}}_0^T\ \tilde{\boldsymbol{\psi}}^{h^{(1)1}T}\right],\\
\tilde{\boldsymbol{\psi}}^{h^{(1)1}T}=\tilde{\boldsymbol{\psi}}^{\,h^{(1)1}T}(s)=\left[\mathbf{h}^{(1)1T}\ \mathbf{h}^{(1)1'T}\right]=\left[u_{1x},\ u_{2y},\ u'_{1x},\ u'_{2y}\right].
\end{gathered}
\tag{11}
$$

For Model 2:

$$
\begin{aligned}
&\tilde{\boldsymbol{\psi}}_2^T=\tilde{\boldsymbol{\psi}}_2^T(s)=\left[\tilde{\boldsymbol{\psi}}_1^T\ \tilde{\boldsymbol{\psi}}^{h^{(2)}T}\right],\quad \tilde{\boldsymbol{\psi}}^{h^{(2)}T}=\left[\mathbf{h}^{(2)T}\ \mathbf{h}^{(2)'T}\right],\\
&\mathbf{h}^{(2)T}=\left[u_{1x^2}\ \ u_{1xy}\ u_{1y^2}\ u_{2x^2}\ \ u_{2xy}\ u_{2y^2}\ u_{3x^2}\ \ u_{3xy}\ u_{3y^2}\right],\\
&\mathbf{h}^{(2)'T}=\left[\ u'_{1x^2}\ \ u'_{1xy}\ u'_{1y^2}\ u'_{2x^2}\ \ u'_{2xy}\ u'_{2y^2}\ u'_{3x^2}\ \ u'_{3xy}\ u'_{3y^2}\right].
\end{aligned}
\tag{12}
$$

For Model 3:

$$
\begin{gathered}
\tilde{\boldsymbol{\psi}}_3^T=\tilde{\boldsymbol{\psi}}_3^T(s)=\left[\tilde{\boldsymbol{\psi}}_1^T\ \tilde{\boldsymbol{\psi}}^{h^{(2)}T}\ \ \tilde{\boldsymbol{\psi}}^{h^{(3)}T}\right],\\
\tilde{\boldsymbol{\psi}}_3^T=\left[\tilde{\boldsymbol{\psi}}_2^T\ \ \tilde{\boldsymbol{\psi}}^{h^{(3)}T}\right],\quad \tilde{\boldsymbol{\psi}}^{h^{(3)}T}=\tilde{\boldsymbol{\psi}}^{h^{(3)}T}(s)=\left[\mathbf{h}^{(3)T}\ \mathbf{h}^{(3)'T}\right],\\
\mathbf{h}^{(3)T}=\left[u_{1x^3}\ \ u_{1x^2y}\ u_{1xy^2}\ u_{1y^3}\ \ u_{2x^3}\ \ u_{2x^2y}\ u_{2xy^2}\ u_{2y^3}\ \ u_{3x^3}\ \ u_{3x^2y}\ u_{3xy^2}\ u_{3y^3}\ \right].
\end{gathered}
\tag{13}
$$

For higher approximations we write:

$$
\tilde{\boldsymbol{\psi}}_m^T=\left[\tilde{\boldsymbol{\psi}}_{m-1}^T\ \ \tilde{\boldsymbol{\psi}}^{h^{(m)}T}\right],\qquad \tilde{\boldsymbol{\psi}}^{h^{(m)}T}=\tilde{\boldsymbol{\psi}}^{h^{(m)}T}(s)=\left[\mathbf{h}^{(m)T}\ \mathbf{h}^{(m)'T}\right].
\tag{14}
$$

Additional director functions are listed in Appendix A.

Based on the above, the deformation vector can be concisely written in the following form for the m-th model

$$\boldsymbol{\varepsilon} = \begin{bmatrix} \varepsilon_1 \\ \varepsilon_2 \\ \varepsilon_3 \\ \gamma_{12} \\ \gamma_{13} \\ \gamma_{23} \end{bmatrix} = [\boldsymbol{\Gamma}_1 \;\; \boldsymbol{\Gamma}_{h^{(2)}} \; ... \; \boldsymbol{\Gamma}_{h^{(m-1)}} \; \boldsymbol{\Gamma}_{h^{(m)}} \,] \begin{bmatrix} \tilde{\boldsymbol{\psi}}_1 \\ \tilde{\boldsymbol{\psi}}^{h^{(2)}} \\ ... \\ \tilde{\boldsymbol{\psi}}^{h^{(m-1)}} \\ \tilde{\boldsymbol{\psi}}^{h^{(m)}} \end{bmatrix} = \boldsymbol{\Gamma}_m \begin{bmatrix} \tilde{\boldsymbol{\psi}}_{m-1} \\ \tilde{\boldsymbol{\psi}}^{h^{(m)}} \end{bmatrix} = \boldsymbol{\Gamma}_m \tilde{\boldsymbol{\psi}}_m, \tag{15}$$

where $\boldsymbol{\Gamma}_m(x, y)$ is generated based on the derivation relations under (9) and the field functions in $\tilde{\boldsymbol{\psi}}_m(s)$. We will approximate based on the p-version finite element

$$\tilde{\boldsymbol{\psi}}_m(s) = \mathbf{G}_m^{total}(s)\mathbf{q}^m + \boldsymbol{\Phi}_{mp}^{total}(s)\mathbf{a}^{mp} \tag{16}$$

where $\mathbf{q}^m$ comprises the nodal values, $\mathbf{a}^{mp}$ is the vector of parameters related to the internal functions, $\mathbf{G}_m^{total}(s)$, $\boldsymbol{\Phi}_{mp}^{total}(s)$ are the approximation matrices. Figure 3 shows the approximation of an arbitrary function h.

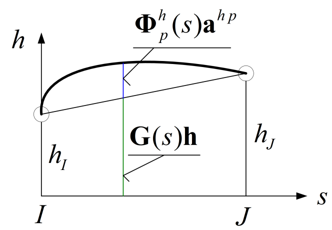

Figure 3. Approximation of field functions within a finite element

$\mathbf{G}(s)\mathbf{h}$ describes the linear change along the rod, while $\boldsymbol{\Phi}_p^h(s)\ \mathbf{a}^{h\,p}$ provides the approximation with a higher degree (maximum p-th degree) polynomial, as indicated in Figure 3. The nodal values h_I, h_J and the additional constants in the vector $\mathbf{a}^{h\,p}$ are the unknowns. The derivation of matrices and vectors in (16) is included in Appendix B.

2.4. **Stresses.** The six independent elements of the stress tensor define the stress vector $\boldsymbol{\sigma}$ of size (6×1):

$$\boldsymbol{\sigma} = \mathbf{D}\,\boldsymbol{\varepsilon} \tag{17}$$

where $\mathbf{D}$ is the matrix of the material constants.

2.4.1. *In the case of Model-0 this is simplified.* It has the following form

$$\boldsymbol{\varepsilon}^T = [\varepsilon_3\ \gamma_{13}\ \gamma_{23}], \quad \boldsymbol{\sigma}^T = [\sigma_3\ \tau_{13}\ \tau_{23}], \quad \mathbf{D} = \langle E\ G\ G \rangle \ \text{ diagonal matrix} \tag{18}$$

where E is the Young's modulus, G is the shear modulus.

2.4.2. *Model-1,...,6d.* Then we have

$$\boldsymbol{\varepsilon}^T = [\varepsilon_1\ \varepsilon_2\ \varepsilon_3\ \gamma_{12}\ \gamma_{13}\ \gamma_{23}]\,, \quad \boldsymbol{\sigma}^T = [\sigma_1\ \sigma_2\ \sigma_3\ \tau_{12}\tau_{13}\ \tau_{23}]\,. \tag{19}$$

For these cases matrix $\mathbf{D}$ is a (6×6) material constant matrix corresponding to the 3D state of stress.

2.5. **Potential energy.** The total potential energy is [1] is given by

$$\Pi_p = \frac{1}{2}\int\limits_V \boldsymbol{\varepsilon}^T \mathbf{D}\,\boldsymbol{\varepsilon}\,dV - W^{work} = \frac{1}{2}\int\limits_L \tilde{\boldsymbol{\psi}}_m^T \Big(\int\limits_S \boldsymbol{\Gamma}_m^T \mathbf{D}\,\Gamma_m\,dS\Big)\tilde{\boldsymbol{\psi}}_m ds - W^{work}, \tag{20}$$

where W^{work} is the work of the external load and the integral over the volume was written as the product of two integrals, one over the length coordinate s, the other over the the cross section S. The integral over the cross section is a function of s,

$$\tilde{\mathbf{D}}_m = \int\limits_S \boldsymbol{\Gamma}_m^T \mathbf{D}\,\boldsymbol{\Gamma}_m\,dS. \qquad m = 1, \ldots, 6 \tag{21}$$

Thus the potential energy is

$$\Pi_p = \frac{1}{2}\int\limits_L \tilde{\boldsymbol{\psi}}_m^T\,\tilde{\boldsymbol{D}}_m\,\tilde{\boldsymbol{\psi}}_m ds - W^{work}. \qquad m = 1, \ldots, 6 \tag{22}$$

The integration should be performed over the domain of s. Using the relations

$$\mathbf{q} = \mathbf{q}^m,\ \mathbf{a} = \mathbf{a}^{mp},\quad \tilde{\mathbf{D}} = \tilde{\mathbf{D}}_m = \int\limits_S \boldsymbol{\Gamma}_m^T \mathbf{D} \boldsymbol{\Gamma}_m\,dS,\quad \mathbf{G} = \mathbf{G}_m^{total} \text{ and } \boldsymbol{\Phi} = \boldsymbol{\Phi}_{mp}^{total}$$

the potential energy can be rewritten into the form

$$\Pi_p = \frac{1}{2}\int\limits_L (\mathbf{q}^T\mathbf{G}^T + \mathbf{a}^T\boldsymbol{\Phi}^T)\,\tilde{\mathbf{D}}\,(\mathbf{G}\mathbf{q} + \boldsymbol{\Phi}\mathbf{a})\,ds - W^{work} = U - W^{work} \tag{23}$$

from which the functional form of the stiffness matrix is yielded as

$$\mathbf{K} = \begin{bmatrix} \mathbf{K}_{qq} & \mathbf{K}_{qa} \\ \mathbf{K}_{aq} & \mathbf{K}_{aa} \end{bmatrix}, \quad \mathbf{K}_{qq} = \int\limits_L \mathbf{G}^T\,\tilde{\mathbf{D}}\,\mathbf{G}\,ds, \tag{24a}$$

$$\mathbf{K}_{aa} = \int\limits_L \boldsymbol{\Phi}^T\,\tilde{\mathbf{D}}\,\boldsymbol{\Phi}\,ds, \quad \mathbf{K}_{qa} = \int\limits_L \mathbf{G}^T\,\tilde{\mathbf{D}}\,\boldsymbol{\Phi}\,ds = \mathbf{K}_{aq}^T. \tag{24b}$$

The reduced load vector is given by $\mathbf{f}^T = \left[\mathbf{f}_q^T\ \mathbf{f}_a^T\right]$.

Finally, eliminating the internal variables, the reduced stiffness matrix and load vector are obtained:

$$\mathbf{K}_{red} = \mathbf{K}_{qq} - \mathbf{K}_{qa}(\mathbf{K}_{aa})^{-1}\mathbf{K}_{aq}, \quad \mathbf{f}_{red} = \mathbf{f}_q - \mathbf{K}_{qa}(\mathbf{K}_{aa})^{-1}\mathbf{f}_a. \tag{25}$$

The internal variables are recovered in the post-solution process using the relationship

$$\mathbf{a} = (\mathbf{K}_{aa})^{-1}\mathbf{f}_a - (\mathbf{K}_{aa})^{-1}\mathbf{K}_{aq}\mathbf{q}. \tag{26}$$

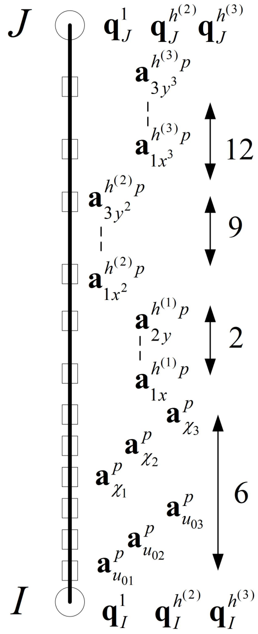

Figure 4. Unknowns associated with the external and internal nodes of the finite element belonging to the $h3$ model

2.6. **The load vectors.**

1. In the case of the $h0$ model the applied loads, as well as the stress resultants, are functions of the center line coordinate.
2. In the case of the $h1, h2, h3, \ldots$ models, we calculate the work of the loads distributed on the surface. The process is illustrated for the $h3$ model in the following. The approximate displacement field for this model is calculated based on (4). Collecting the functions depending on s, we write:

$$\boldsymbol{\psi}_3^{displ} = \boldsymbol{\psi}_3^{displ}(s) = \begin{bmatrix} \mathbf{u}_0(s) \\ \boldsymbol{\chi}(s) \\ \mathbf{h}^{(1)1}(s) \\ \mathbf{h}^{(2)}(s) \\ \mathbf{h}^{(3)}(s) \end{bmatrix} = \begin{bmatrix} \mathbf{h}^{(1)}(s) \\ \mathbf{h}^{(2)}(s) \\ \mathbf{h}^{(3)}(s) \end{bmatrix} = \mathbf{R}_{red}^3 \begin{bmatrix} \mathbf{h}^{(1)}(s) \\ \mathbf{h}^{(1)'}(s) \\ \mathbf{h}^{(2)}(s) \\ \mathbf{h}^{(2)'}(s) \\ \mathbf{h}^{(3)}(s) \\ \mathbf{h}^{(3)'}(s) \end{bmatrix} = \mathbf{R}_{red}^3 \tilde{\boldsymbol{\psi}}_3(s), \quad (27)$$

where the operator $\mathbf{R}_{red(29,58)}^3$ produces the displacements $\boldsymbol{\psi}_3^{displ}$ from the $\boldsymbol{\psi}_3$ vector, including the derivatives. Therefore the displacement vector defined in (4), taking into account (27), is

$$\mathbf{u} = \mathbf{u}(x, y, s) = \left[\mathbf{U}_{(1)}\ \mathbf{U}_{(2)}\ \mathbf{U}_{(3)}\right] \boldsymbol{\psi}_3^{displ} = \\ = \mathbf{U}^3(x, y)\boldsymbol{\psi}_3^{displ}(s) = \mathbf{U}^3(x, y)\mathbf{R}_{red}^3\tilde{\boldsymbol{\psi}}_3(s). \quad (28)$$

Furthermore, in a view of (16) we have

$$\tilde{\boldsymbol{\psi}}_3(s) = \mathbf{G}^{total}(s)\,\mathbf{q}^{total} + \boldsymbol{\Phi}^{total}(s)\,\mathbf{a}^{total}. \tag{29}$$

Hence the work of the load acting on the surface S_{load} is

$$W^{work} = \int\limits_{S_{load}} \tilde{\boldsymbol{\psi}}_3^T(s)\mathbf{R}_{red}^{3,T}\,\mathbf{U}^{3,T}(x,y)\,\mathbf{p}_{load}(x,y,s)\,dS, \tag{30}$$

from which the reduced load vectors are calculated. When the load is a function of x, y (i.e. the load acts on the cross-section of the bar, marked I or J) and the cross section of the body is rectangular, with dimensions a, b in the x and y directions, then the distributed load can be written as

$$\mathbf{p}_{load} = \begin{bmatrix} \tau_{13}^0\left(1-\left(\frac{x}{a/2}\right)^2\right) \\ \tau_{23}^0\left(1-\left(\frac{y}{b/2}\right)^2\right) \\ \sigma^0 - \frac{\sigma^+}{b/2}y \end{bmatrix} \tag{31}$$

where $\tau_{13}^0,\ \tau_{23}^0,\ \sigma^0,\ \sigma^+$ are given quantities. Then the work of the load is

$$W^{work} = \tilde{\boldsymbol{\psi}}_3^T(s_{I(J)})\mathbf{R}_{red}^{3,T}\int\limits_{S_{I(J)}}\mathbf{U}^{3,T}(x,y)\,\mathbf{p}_{load}(x,y)\,dS_{xy}\,. \tag{32}$$

With (32) the reduced load vectors are

$$\begin{aligned}\mathbf{f}_q &= \left(\mathbf{G}^{total,T}(s_{I(J)})\right)\mathbf{R}_{red}^{3,T}\int\limits_{S_{I(J)}}\mathbf{U}^{3,T}(x,y)\,\mathbf{p}_{load}(x,y)\,dS_{xy}\,,\\ \mathbf{f}_a &= \left(\boldsymbol{\Phi}^{total,T}(s_{I(J)})\right)\mathbf{R}_{red}^{3,T}\int\limits_{S_{I(J)}}\mathbf{U}^{3,T}(x,y)\,\mathbf{p}_{load}(x,y)\,dS_{xy}\,.\end{aligned} \tag{33}$$

If the load is exerted on a planar surface defined by $x = -a/2$ then

$$W^{work} = \int\limits_{S_{load}} \tilde{\boldsymbol{\psi}}_3^T(s)\mathbf{R}_{red}^{3,T}\,\mathbf{U}^{3,T}(x=-a/2,y)\,\mathbf{p}_{load}(y,s)\,dS_{ys}. \tag{34}$$

The procedure is analogous for the other hierarchic models.

2.7. **Treatment of elastic foundation.** Let us assume that on the surface $y = b/2$ a ring-shaped body is in contact with a Winkler-type foundation characterized by spring constant c. Then the strain energy is

$$U^{found} = \frac{1}{2}\int\limits_{S_{found}} u_y(x,y=b/2,s)\,c u_y(x,y=b/2,s)\,dS_{xs}\,. \tag{35}$$

Therefore, in view of the approximation of $\mathbf{u}(x,y,s)$ under (28) we get

$$u_y = \mathbf{u}(x,y,s)^T\mathbf{e}_2 = \left(\mathbf{u}(x,y,s)^T\mathbf{e}_2\right)^T = \mathbf{e}_2^T\mathbf{u}(x,y,s) = \mathbf{u}(x,y,s)^T\begin{bmatrix}0\\1\\0\end{bmatrix} =$$

$$[0\ 1\ 0]\,\mathbf{u}(x,y,s) = \tilde{\boldsymbol{\psi}}_3^T(s)\mathbf{R}_{red}^{3,T}\mathbf{U}^{3,T}(x,y)\begin{bmatrix}0\\1\\0\end{bmatrix} = [0\ 1\ 0]\,\mathbf{U}^3(x,y)\mathbf{R}_{red}^3\tilde{\boldsymbol{\psi}}_3(s), \quad (36)$$

that is

$$U^{found} = \frac{1}{2}\int\limits_{S_{found}} \tilde{\boldsymbol{\psi}}_3^T(s)\mathbf{R}_{red}^{3,T}\mathbf{U}^{3,T}(x,y=b/2)\begin{bmatrix}0&0&0\\0&c&0\\0&0&0\end{bmatrix}\mathbf{U}^3(x,y=b/2)\mathbf{R}_{red}^3\tilde{\boldsymbol{\psi}}_3(s)dS_{xs}\,. \quad (37)$$

Using (29), omitting the upper index and performing the integrations, the energy is written in the form

$$U^{found} = \frac{1}{2}\left[\mathbf{q}^T\ \mathbf{a}^T\right]\begin{bmatrix}\mathbf{C}_{qq} & \mathbf{C}_{qa}\\ \mathbf{C}_{aq} & \mathbf{C}_{aa}\end{bmatrix}\begin{bmatrix}\mathbf{q}\\ \mathbf{a}\end{bmatrix}, \quad (38)$$

where the stiffness matrix of the elastic support is

$$\mathbf{C} = \begin{bmatrix}\mathbf{C}_{qq} & \mathbf{C}_{qa}\\ \mathbf{C}_{aq} & \mathbf{C}_{aa}\end{bmatrix}$$

in which

$$\mathbf{C}_{qq} = \int\limits_{S_{xs}}\mathbf{G}^T\mathbf{W}\,\mathbf{G}\,dS_{xs}\,, \quad \mathbf{C}_{aa} = \int\limits_{S_{xs}}\mathbf{\Phi}^T\,\mathbf{W}\,\mathbf{\Phi}\,dS_{xs}\,, \quad \mathbf{C}_{qa} = \int\limits_{S_{xs}}\mathbf{G}^T\,\mathbf{W}\,\mathbf{\Phi}dS_{xs} = \mathbf{C}_{aq}^T$$

and

$$\mathbf{W} = \mathbf{W}\,(x,y=b/2) = \mathbf{R}_{red}^{3,T}\mathbf{U}^{3,T}(x,y=b/2)\begin{bmatrix}0&0&0\\0&c&0\\0&0&0\end{bmatrix}\mathbf{U}^3(x,y=b/2)\mathbf{R}_{red}^3.$$

3. Formulation of frictionless contact problem

3.1. **General equations.** The line of thought in this subsection is based on [38, 39, 50, 51]. Let the displacement of the bodies in the normal direction of contact $\mathbf{n}_c$ be $u^i = \mathbf{u}^i \cdot \mathbf{n}_c$, $i = 1, 2$, and g be the initial gap in the contact region S_c – see Figure 5.

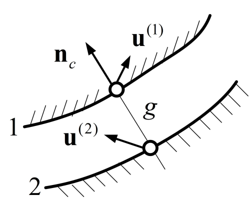

Figure 5. Bodies in contact. Notations

There is contact when $d = u_n^{(1)} - u_n^{(2)} + g = 0$ and $p_n \geqslant 0$, while a gap is present if $d = u_n^{(1)} - u_n^{(2)} + g > 0$ and $p_n = 0$, where d is the gap formed after deformation and p_n is the contact pressure.

The $p_n d = 0$ condition is fulfilled over the entire S_c domain. Solving the contact problem with the augmented Lagrange multiplier method [17, 28, 32, 42], it is necessary to incorporate the contact penalty energy:

$$U^{cont} = \frac{1}{2}\int\limits_{S_c} d^- \, c_n \, d^- \, dS_c = \frac{1}{2}\int\limits_{S_c} (u_n^{(1)} - u_n^{(2)} + g) c_n \, (u_n^{(1)} - u_n^{(2)} + g) \, dS_c \tag{39}$$

and the Lagrangian term:

$$W_{aug} = \int\limits_{S_c} p_n d \, dS = \int\limits_{S_c} p_n (u_n^{(1)} - u_n^{(2)} + g) dS, \tag{40}$$

where $d^- \leq 0$, $c_n >> 0$ is the penalty parameter. The displacement in the normal direction is given by

$$u_n^{(i)} = \mathbf{n}_c \cdot \mathbf{u}^{(i)} = \mathbf{n}^T \mathbf{u}^{(i)}, \qquad i = 1, 2.$$

The total energy, the minimum of which is sought subject to the stated inequalities, is:

$$L_{aug} = \Pi_p - W_{aug} + U^{cont}. \tag{41}$$

Considering the relation $u_n^{(i)} = \mathbf{n}_c \cdot \mathbf{u}^{(i)} = \mathbf{n}^T \mathbf{u}^{(i)}$ and using (28), (29) for the displacement of the i-th body in the normal direction on the surface $y_b^{(i)}$(the formulae are general, so we ignore the reference to the $h3$ model, the index 3), we get

$$\begin{aligned} u_n^{(i)} &= \mathbf{n}^T \mathbf{U}^{(i)}(x, y_b^{(i)}) \mathbf{R}_{red} \left(\mathbf{G}^{(i)}(s) \mathbf{q}^{(i)} + \mathbf{\Phi}^{(i)}(s) \mathbf{a}^{(i)} \right) = \\ &= \mathbf{n}^T \tilde{\mathbf{U}}^{(i)}(x, y_b^{(i)}) \left(\mathbf{G}^{(i)}(s) \mathbf{q}^{(i)} + \mathbf{\Phi}^{(i)}(s) \mathbf{a}^{(i)} \right) \end{aligned} \tag{42}$$

and, defining $\mathbf{C}_n = c_n \, \mathbf{n}^T \mathbf{n}$, the penalty energy given in (39), neglecting the constant term from the initial gap, is written in compact form:

$$U^{cont} = \frac{1}{2} \left[\mathbf{a}^T \mathbf{q}^T \right] \left(\begin{bmatrix} \mathbf{C}_{qq} & \mathbf{C}_{qa} \\ \mathbf{C}_{aq} & \mathbf{C}_{aa} \end{bmatrix} \begin{bmatrix} \mathbf{q} \\ \mathbf{a} \end{bmatrix} - 2 \begin{bmatrix} \mathbf{f}_{cq} \\ \mathbf{f}_{ca} \end{bmatrix} \right) = \frac{1}{2} \tilde{\mathbf{q}}^T \left(\tilde{\mathbf{C}} \, \tilde{\mathbf{q}} - 2\tilde{\mathbf{f}} \right), \tag{43}$$

where

$$\mathbf{q}^T = \left[\mathbf{q}^{(1)T} \; \mathbf{q}^{(2)T} \right], \qquad \mathbf{a}^T = \left[\mathbf{a}^{(1)T} \; \mathbf{a}^{(2)T} \right],$$

$$\mathbf{C}_{qq} = \int\limits_{S_c} \begin{bmatrix} \mathbf{G}^{(1)T} \tilde{\mathbf{U}}^{(1)T} \mathbf{C}_n \tilde{\mathbf{U}}^{(1)} \mathbf{G}^{(1)} & -\mathbf{G}^{(1)T} \tilde{\mathbf{U}}^{(1)T} \mathbf{C}_n \tilde{\mathbf{U}}^{(2)} \mathbf{G}^{(2)} \\ -\mathbf{G}^{(2)T} \tilde{\mathbf{U}}^{(2)T} \mathbf{C}_n \tilde{\mathbf{U}}^{(1)} \mathbf{G}^{(1)} & \mathbf{G}^{(2)T} \tilde{\mathbf{U}}^{(2)T} \mathbf{C}_n \tilde{\mathbf{U}}^{(2)} \mathbf{G}^{(2)} \end{bmatrix} dS_c \, ,$$

$$\mathbf{f}_{cq} = -\int\limits_{S_c} c_n \begin{bmatrix} \mathbf{G}^{(1)T} \tilde{\mathbf{U}}^{(1)T} \mathbf{n} g \\ -\mathbf{G}^{(2)T} \tilde{\mathbf{U}}^{(2)T} \mathbf{n} g \end{bmatrix} dS_c \, ,$$

$$\mathbf{C}_{aq} = \mathbf{C}_{qa}^T = \int\limits_{S_c} \begin{bmatrix} \mathbf{\Phi}^{(1)T} \tilde{\mathbf{U}}^{(1)T} \mathbf{C}_n \tilde{\mathbf{U}}^{(1)} \mathbf{G}^{(1)} & -\mathbf{\Phi}^{(1)T} \tilde{\mathbf{U}}^{(1)T} \mathbf{C}_n \tilde{\mathbf{U}}^{(2)} \mathbf{G}^{(2)} \\ -\mathbf{\Phi}^{(2)T} \tilde{\mathbf{U}}^{(2)T} \mathbf{C}_n \tilde{\mathbf{U}}^{(1)} \mathbf{G}^{(1)} & \mathbf{\Phi}^{(2)T} \tilde{\mathbf{U}}^{(2)T} \mathbf{C}_n \tilde{\mathbf{U}}^{(2)} \mathbf{G}^{(2)} \end{bmatrix} dS_c \, ,$$

$$\mathbf{C}_{aa} = \int\limits_{S_c} \begin{bmatrix} \mathbf{\Phi}^{(1)T}\tilde{\mathbf{U}}^{(1)T}\mathbf{C}_n\tilde{\mathbf{U}}^{(1)}\mathbf{\Phi}^{(1)} & -\mathbf{\Phi}^{(1)T}\tilde{\mathbf{U}}^{(1)T}\mathbf{C}_n\tilde{\mathbf{U}}^{(2)}\mathbf{\Phi}^{(2)} \\ -\mathbf{\Phi}^{(2)T}\tilde{\mathbf{U}}^{(2)T}\mathbf{C}_n\tilde{\mathbf{U}}^{(1)}\mathbf{\Phi}^{(1)} & \mathbf{\Phi}^{(2)T}\tilde{\mathbf{U}}^{(2)T}\mathbf{C}_n\tilde{\mathbf{U}}^{(2)}\mathbf{\Phi}^{(2)} \end{bmatrix} dS_c\,,$$

$$\mathbf{f}_{ca} = -\int\limits_{S_c} c_n \begin{bmatrix} \mathbf{\Phi}^{(1)T}\tilde{\mathbf{U}}^{(1)T}\mathbf{n}g \\ -\mathbf{\Phi}^{(2)T}\tilde{\mathbf{U}}^{(2)T}\mathbf{n}g \end{bmatrix} dS_c\,,$$

and $\tilde{\mathbf{C}}$, $\tilde{\mathbf{f}}$ are the stiffness matrix and load vector of the contact element, respectively. When $u_n^{(1)} = 0$, then we get the stiffness matrix of the Winkler-type foundation for body 2.

The work term corresponding to augmentation is:

$$W_{aug} = \int\limits_{S_c} p_n d\, dS = \int\limits_{S_c} p_n(\mathbf{q}^{(1),T}\mathbf{G}^{(1)T}\tilde{\mathbf{U}}^{(1)T}\mathbf{n} - \mathbf{q}^{(2),T}\mathbf{G}^{(2)T}\tilde{\mathbf{U}}^{(2)T}\mathbf{n} + g)dS +$$
$$+ \int\limits_{S_c} p_n(\mathbf{a}^{(1),T}\mathbf{\Phi}^{(1)T}\tilde{\mathbf{U}}^{(1)T}\mathbf{n} - \mathbf{a}^{(2),T}\mathbf{\Phi}^{(2)T}\tilde{\mathbf{U}}^{(2)T}\mathbf{n})dS,$$

that is

$$W_{aug} = \mathbf{q}^T\mathbf{f}_{aug,q} + \mathbf{a}^T\mathbf{f}_{aug,a}\,, \tag{44a}$$

where

$$\mathbf{f}_{aug,q} = \begin{bmatrix} \int\limits_{S_c} p_n\mathbf{G}^{(1)T}\tilde{\mathbf{U}}^{(1)T}\mathbf{n}\, dS \\ -\int\limits_{S_c} p_n\mathbf{G}^{(2)T}\tilde{\mathbf{U}}^{(2)T}\mathbf{n}\, dS \end{bmatrix}, \quad \mathbf{f}_{aug,a} = \begin{bmatrix} \int\limits_{S_c} p_n\mathbf{\Phi}^{(1)T}\tilde{\mathbf{U}}^{(1)T}\mathbf{n}\, dS \\ -\int\limits_{S_c} p_n\mathbf{\Phi}^{(2)T}\tilde{\mathbf{U}}^{(2)T}\mathbf{n}\, dS \end{bmatrix}. \tag{44b}$$

In the iterative solution process the contact pressure is calculated from the following formula using Macaulay brackets

$$p_n^{(j+1)} = \left\langle p_n^{(j)} - c_n d^{(j)} \right\rangle, \qquad x^{(j+1)} = \left\langle \frac{x^{(j)} + \left|x^{(j)}\right|}{2} \right\rangle. \tag{45}$$

The iteration process is started by solving the problem using the penalty method and continued by incrementing the pressure where the term in parenthesis is positive, and setting the value of c_n to zero where it is negative. This gives us the modified contact stiffness and load vector. The iteration process is generally stable when the c_n value is sufficiently small.

3.2. **Model in the global coordinate system.**

3.2.1. *Hierarchical bar elements in cases when the displacement field is approximated by Taylor or Legendre polynomials.* The displacement vector in the XYZ global coordinate system is written as:

$$\mathbf{u} = u\,\mathbf{e}_X + v\,\mathbf{e}_Y + w\,\mathbf{e}_Z. \tag{46}$$

The displacement in the cross section of a rod is approximated by the function $\mathbf{U}_{(m)}(\xi,\eta)$, in the longitudinal direction it is approximated by the function $\mathbf{h}^{(m)}(\zeta)$. The displacement vector is the product of the two functions:

$$\mathbf{u} = \mathbf{u}(\xi,\eta,\zeta) = \sum_{m=1}^{M} \bar{\mathbf{h}}^{(m)}(\xi,\eta,\zeta) = \sum_{m=1}^{M} \mathbf{U}_{(m)}(\xi,\eta)\,\mathbf{h}^{(m)}(\zeta), \tag{47}$$

where $-1 \le \xi \le 1$, $-1 \le \eta \le 1$, $-1 \le \zeta \le 1$ are the coordinates of the standard hexahedral element.

Depending on the degree of the polynomial functions included in the series expansion, we arrive at a sequence of hierarchical rod models, characterized by polynomials of degree Tm or Lm. At a given level, the longitudinal distribution of the displacement field is determined by the highest power of the polynomial in the definition of $\mathbf{h}^{(m)}(\zeta)$. The maximum of the degree will be denoted by p.

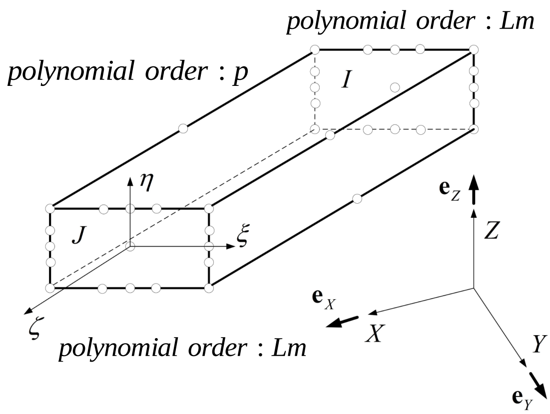

Figure 6. A prismatic rod with a rectangular cross section in the adopted local coordinate system (ξ,η,ζ). I and J are the initial and final cross section labels.

We denote the shape functions containing Lm-order Legendre polynomials [1, 37] describing the director functions by $N_i(\xi,\eta)$, and the longitudinal ones by $\psi^i(\zeta)$. We get

$$u_\tau = \sum_{i=1}^{nLm} N_i(\xi,\eta)\cdot\psi^i_\tau(\zeta), \quad \tau = 1,2,3 \tag{48}$$

which in matrix form is written as

$$u_\tau = \mathbf{N}^\tau(\xi,\eta)\boldsymbol{\psi}_\tau(\zeta), \quad \tau = 1,2,3 \tag{49}$$

where

$$\mathbf{N}^\tau(\xi,\eta) = [N_1(\xi,\eta)\ N_2(\xi,\eta), ..., N_i(\xi,\eta), ..., N_{nLm}(\xi,\eta)]_{(1,nLm)},$$

in which nLm is the number of Legendre polynomials. The $\boldsymbol{\psi}_\tau$ function is approximated as outlined in Figure 7. The displacement of the bodies will be approximated

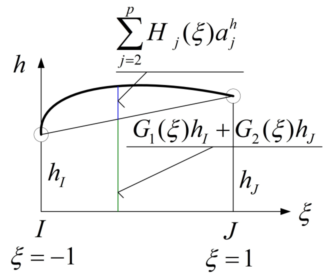

Figure 7. Approximation along the length of the rod for an arbitrary function h

by linear approximation and higher power Legendre functions through the values in the nodes I and J of the element. In concise form:

$$\psi_\tau^i = \psi_\tau^i(\zeta) = \frac{1}{2}(1-\zeta)u_\tau^{i,I} + \frac{1}{2}(1+\zeta)u_\tau^{i,J} + \sum_{j=2}^{p} H_j(\zeta)a_\tau^{i,j}, \quad i=1,...,nLm, \quad \tau=1,2,3 \tag{50a}$$

$$\psi_\tau^i = \psi_\tau^i(\zeta) = \left[\frac{1}{2}(1-\zeta) \ \ \frac{1}{2}(1+\zeta)\right]\left[\begin{array}{c} u_\tau^{i,I} \\ u_\tau^{i,J} \end{array}\right] + \sum_{j=2}^{p} H_j(\zeta)a_\tau^{i,j}, \quad i=1,...,nLm, \quad \tau=1,2,3 \tag{50b}$$

$$\psi_\tau^i = \psi_\tau^i(\zeta) = \tilde{\mathbf{g}}(\zeta)\mathbf{q}_\tau^i + \tilde{\mathbf{h}}(\zeta)\mathbf{a}_\tau^i, \quad i=1,...,nLm, \quad \tau=1,2,3 \tag{50c}$$

It can be seen from the approximation displayed in (50) that one component of the displacement is approximated through $nLm * (p+1)$ parameters. Note that $H_j(\zeta)$ can be obtained from Legendre polynomials $P_j(\zeta)$ using the formula

$$H_j(\zeta) = \frac{1}{\sqrt{2(2j-1)}}(P_j(\zeta) - P_{j-2}(\zeta)),$$

see, for example [1, 37]. In matrix form ($np = p-1$):

$$\begin{aligned}\boldsymbol{\psi}_{\tau(nLm,1)} &= \boldsymbol{\psi}_\tau(\zeta) = \\ &= \tilde{\mathbf{G}}(\zeta)_{(nLm,2\times nLm)}\mathbf{q}_{\tau(2\times nLm,1)} + \tilde{\mathbf{H}}(\zeta)_{(nLm,nLm\times np)}\mathbf{a}_{\tau(nLm\times np,1)}, \quad \tau = 1,2,3\end{aligned} \tag{51}$$

Introducing the following matrix:

$$\underset{(3,3\times nLm)}{\mathbf{N}(\xi,\eta)} = \begin{bmatrix} N_1(\xi,\eta) & 0 & 0 & \dots & N_i(\xi,\eta) & 0 & 0 & \dots \\ 0 & N_1(\xi,\eta) & 0 & \dots & 0 & N_i(\xi,\eta) & 0 & \dots \\ 0 & 0 & N_1(\xi,\eta) & \dots & 0 & 0 & N_i(\xi,\eta) & \dots \end{bmatrix} \tag{52}$$

the displacement vector $\mathbf{u}^T = [u_1\ u_2\ u_3]$ is written in the following form:

$$\mathbf{u} = \mathbf{N}(\xi,\eta)\psi(\zeta). \tag{53}$$

In addition the vector $\boldsymbol{\psi} = \boldsymbol{\psi}(\zeta)$ is:

$$\begin{aligned} &\boldsymbol{\psi}_{(3\times nLm,1)} = \boldsymbol{\psi}(\zeta) = \\ &\quad = \mathbf{G}(\zeta)_{(3\times nLm,6\times nLm)}\mathbf{q}_{(6\times nLm,1)} + \boldsymbol{\Phi}(\zeta)_{(3\times nLm,3\times nLm\times np)}\mathbf{a}_{(3\times nLm\times np,1)} \end{aligned} \tag{54}$$

$$\underset{(1,np)}{\tilde{\mathbf{h}}} = \begin{bmatrix} H_2(\zeta) & H_3(\zeta) & \dots & H_p(\zeta) \end{bmatrix}, \qquad \underset{(nLm,nLm\times np)}{\tilde{\mathbf{H}}(\zeta)} = \begin{bmatrix} \tilde{\mathbf{h}}(\zeta) & & \dots & \\ & \tilde{\mathbf{h}}(\zeta) & \dots & \\ \dots & \dots & \dots & \dots \\ & & \dots & \tilde{\mathbf{h}}(\zeta) \end{bmatrix}, \tag{55a}$$

$$\underset{(2\times nLm,1)}{\mathbf{q}_\tau} = \begin{bmatrix} \mathbf{q}^1 \\ \mathbf{q}^2 \\ \dots \\ \mathbf{q}^{nLm} \end{bmatrix}, \qquad \underset{(nLm\times np,1)}{\mathbf{a}_\tau} = \begin{bmatrix} \mathbf{a}^1 \\ \mathbf{a}^2 \\ \dots \\ \mathbf{a}^{nLm} \end{bmatrix}, \tag{55b}$$

$$\begin{gathered} \underset{(nLm,2\times nLm)}{\tilde{\mathbf{G}}} = \begin{bmatrix} \tilde{G}_{11} & 0 & \cdots & 0 & \tilde{G}_{1,nLm+1} & 0 & \cdots & 0 \\ 0 & \tilde{G}_{22} & \cdots & 0 & 0 & \tilde{G}_{2,nLm+2} & \cdots & 0 \\ \dots & \dots & \dots & \dots & \dots & \dots & \dots & \dots \\ 0 & 0 & \cdots & \tilde{G}_{nLm,nLm} & 0 & 0 & \cdots & \tilde{G}_{nLm,2\times nLm} \end{bmatrix}, \\ \tilde{G}_{11} = \tilde{G}_{22} = \cdots = \tilde{G}_{nLm,nLm} = \frac{1-\zeta}{2}, \\ \tilde{G}_{1,nLm+1} = \tilde{G}_{2,nLm+2} = \cdots = \tilde{G}_{nLm,2\times nLm} = \frac{1+\zeta}{2}, \end{gathered} \tag{55c}$$

$$\begin{gathered} \underset{(3\times nLm,6\times nLm)}{\mathbf{G}} = \\ \begin{bmatrix} G_{11} & 0 & \cdots & 0 & G_{1,3\times nLm+1} & 0 & \cdots & 0 \\ 0 & \tilde{G}_{22} & \cdots & 0 & 0 & \tilde{G}_{2,3\times nLm+2} & \cdots & 0 \\ \dots & \dots & \dots & \dots & \dots & \dots & \dots & \dots \\ 0 & 0 & \cdots & \tilde{G}_{3\times nLm,3\times nLm} & 0 & 0 & \cdots & \tilde{G}_{3\times nLm,6\times nLm} \end{bmatrix}, \\ G_{11} = G_{22} = \cdots = G_{3\times nLm,3\times nLm} = \frac{1-\zeta}{2}, \\ G_{1,3\times nLm+1} = G_{2,3\times nLm+2} = \cdots = G_{3\times nLm,6\times nLm} = \frac{1+\zeta}{2}. \end{gathered} \tag{55d}$$

$$\underset{(3\times nLm,3\times nLm\times np)}{\mathbf{\Phi}(\zeta)} = \begin{bmatrix} H_2 & H_3 & \cdots & H_p & 0 & 0 & \cdots & 0 & \cdots\cdots & 0 & 0 & \cdots & 0 \\ 0 & 0 & \cdots & 0 & H_2 & H_3 & \cdots & H_p & \cdots\cdots & 0 & 0 & \cdots & 0 \\ \cdots & \cdots & \cdots & \cdots & \cdots & \cdots & \cdots & \cdots & \cdots & \cdots & \cdots & \cdots & \cdots \\ 0 & 0 & \cdots & 0 & 0 & 0 & \cdots & 0 & \cdots\cdots & H_2 & H_3 & \cdots & H_p \end{bmatrix}. \tag{55e}$$

The internal coordinates displacement coordinates of the element are approximated via $ND_{hLm}{}^1 = 2\times nLm + nLm\times(p-1) = nLm(p+1)$ parameters. So, the vector $\mathbf{q}_{(6\times nLm,1)}$ contains the coefficients of hLm polynomials interpreted on the I and J planes, while the vector $\mathbf{a}_{(3\times nLm\times np,1)}$ contains the coefficients $a_\tau^{i,j}$ that multiply the polynomials $H_j(\zeta)$, i.e.

$$\underset{(1,6\times nLm)}{\mathbf{q}^T} = \Big[u_1^{1,I}\ u_2^{1,I}\ u_3^{1,I}\ u_1^{2,I}\ u_2^{2,I}\ u_3^{2,I}\ \ldots\ u_1^{nLm,I}\ u_2^{nLm,I}\ u_3^{nLm,I}$$
$$u_1^{1,J}\ u_2^{1,J}\ u_3^{1,J}\ u_1^{2,J}\ u_2^{2,J}\ u_3^{2,J}\ \ldots\ u_1^{nLm,J}\ u_2^{nLm,J}\ u_3^{nLm,J}\Big] \tag{56}$$

$$\underset{(1,3\times nLm\times np)}{\mathbf{a}^T} = \Big[a_1^{1,2}\ \ldots\ a_1^{1,p} a_2^{1,2}\ \ldots\ a_2^{1,p}\ a_3^{1,2} \ldots\ a_3^{1,p}\ \ldots$$
$$a_1^{nLm,2}\ \ldots\ a_1^{nLm,p}\ a_2^{nLm,2}\ \ldots\ a_2^{nLm,p}\ a_3^{nLm,2}\ \ldots\ a_3^{nLm,p}\Big] \tag{57}$$

Using the notation $u = u_1$, $v = u_2$ $w = u_3$ the components of the strain tensor are calculated as follows:

$$\begin{gathered} \varepsilon_X = \frac{\partial u}{\partial X}, \quad \varepsilon_Y = \frac{\partial v}{\partial Y}, \quad \varepsilon_Z = \frac{\partial w}{\partial Z}, \\ \gamma_{XY} = \frac{\partial u}{\partial Y} + \frac{\partial v}{\partial X}, \quad \gamma_{YZ} = \frac{\partial v}{\partial Z} + \frac{\partial W}{\partial Y}, \quad \gamma_{ZX} = \frac{\partial w}{\partial X} + \frac{\partial u}{\partial Z}. \end{gathered} \tag{58}$$

Since the displacement field is approximated in the local system ξ, η, ζ, it will be necessary to calculate the derivative of the displacement u in the global system:

$$\partial_G \mathbf{u} = \begin{bmatrix} \frac{\partial u}{\partial X} \\ \frac{\partial u}{\partial Y} \\ \frac{\partial u}{\partial Z} \end{bmatrix} = \mathbf{J}^{-1} \begin{bmatrix} \frac{\partial u}{\partial \xi} \\ \frac{\partial u}{\partial \eta} \\ \frac{\partial u}{\partial \zeta} \end{bmatrix} = \mathbf{J}^{-1}\partial_L \mathbf{u}\,,$$

where $\mathbf{J}^{-1}$ is the inverse of Jacobian matrix $\mathbf{J}$:

$$\mathbf{J} = \begin{bmatrix} \frac{\partial X}{\partial \xi} & \frac{\partial Y}{\partial \xi} & \frac{\partial Z}{\partial \xi} \\ \frac{\partial X}{\partial \eta} & \frac{\partial Y}{\partial \eta} & \frac{\partial Z}{\partial \eta} \\ \frac{\partial X}{\partial \zeta} & \frac{\partial Y}{\partial \zeta} & \frac{\partial Z}{\partial \zeta} \end{bmatrix}. \tag{59}$$

We remark that $\mathbf{J}$ is calculated from the mapping functions. For later consideration we shall introduce the following notations:

$$\partial_\xi N(\xi,\eta) = N_{,\xi}(\xi,\eta), \quad \partial_\eta N(\xi,\eta) = N_{,\eta}(\xi,\eta), \quad \partial_\zeta \tilde{G}(\zeta) = \tilde{G}_{,\zeta}(\zeta), \quad \partial_\zeta \tilde{H}(\zeta) = \tilde{H}_{,\zeta}(\zeta) \tag{60}$$

The derivatives of the displacement fields in the local system are:

$$
\begin{aligned}
u_{,\xi} &= \frac{\partial u}{\partial \xi} = \mathbf{N}_{,\xi}(\xi,\eta)(\tilde{\mathbf{G}}(\zeta)\mathbf{q}^u + \tilde{\mathbf{H}}(\zeta)\mathbf{a}^u), \quad u = u_1 \leftrightarrow v = u_2 \leftrightarrow w = u_3 \\
u_{,\eta} &= \frac{\partial u}{\partial \eta} = \mathbf{N}_{,\eta}(\xi,\eta)(\tilde{\mathbf{G}}(\zeta)\mathbf{q}^u + \tilde{\mathbf{H}}(\zeta)\mathbf{a}^u), \quad u = u_1 \leftrightarrow v = u_2 \leftrightarrow w = u_3 \\
u_{,\zeta} &= \frac{\partial u}{\partial \zeta} = \mathbf{N}(\xi,\eta)(\tilde{\mathbf{G}}_{,\zeta}(\zeta)\mathbf{q}^u + \tilde{\mathbf{H}}_{,\zeta}(\zeta)\mathbf{a}^u), \quad u = u_1 \leftrightarrow v = u_2 \leftrightarrow w = u_3
\end{aligned}
\tag{61}
$$

Based on (58), the derivatives of the displacement components are computed in the global coordinate system from which the $3D$ strain tensor and, through application of Hooke's law, the stress tensor are computed.

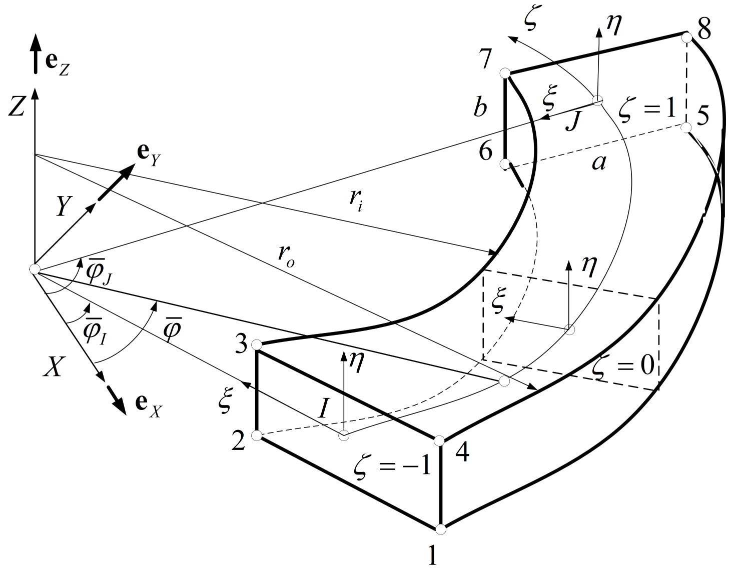

Figure 8. Relationship betweern the local coordinates ξ, η, ζ and the global ones

The mapping for a curved element is illustrated in Figure 8 where the blending technique was used to produce a smooth mapping function [1, 37].

Note that $\bar{\varphi}_m = (\bar{\varphi}_I + \bar{\varphi}_J)/2, \quad \bar{\varphi}_d = (\bar{\varphi}_J - \bar{\varphi}_I)/2, \quad \bar{\varphi} = \bar{\varphi}_m + \zeta\bar{\varphi}_d$.

It is worth comparing the number of unknowns associated with the $3D$ p-version with the hierarchical element: Using the trunk space described [1, 37], each field is approximated with ${ND_{3D}}^1$ unknowns whereas there are ${ND_{hLm}}^1$ unknowns in the hierarchic formulation.

The three displacement fields are approximated using $ND_{hLm} = 3 \times nLm \times 2 + 3 \times nLm \times (p-1) = 3 \times nLm \times (p+1)$ degrees of freedom per element. Of these, $3 \times nLm \times 2$ belong to the boundary points (nodes I and J), the rest are internal functions. For $3D$ elements (hexahedral element), the number of unknowns used to describe one or three fields is ${ND_{3D}}^1$ or ${ND_{3D}}^3$, i.e.,

	$p=2$	3	4	5	6
${ND_{3D}}^1$	20	35	54	79	111
${ND_{3D}}^3$	60	105	162	237	333

For the planar trunk space, the number of unknowns is:

	$p=2$	3	4	5	6	7	8
${ND_{2D}}^1$	8	12	17	23	30	38	47
${ND_{2D}}^2$	16	24	34	46	50	76	94

These relationships also hold when Tm polynomials rather than Lm polynomials are used.

The director functions for the hTm elements are the polynomials constructed by substituting $x \to \xi$, $y \to \eta$ for the monomials of the Pascal triangle (see Appendix A) for the hm element, where $-1 \le \xi \le 1$, $-1 \le \eta \le 1$, i.e. $hm \to hTm$.

Since three-dimensional displacements are approximated by both the hTm and hLm elements, the total number of unknowns is ${ND_{hTm}}^1$ and ND_{hTm}, respectively.

hTm beam element with Taylor expansion

	ht2	ht3	ht4	ht5	ht6	ht7	ht8
${ND_{hTm}}^1$	6(p+1)	10(p+1)	15(p+1)	21(p+1)	28(p+1)	36(p+1)	45(p+1)
ND_{hTm}	18(p+1)	30(p+1)	45(p+1)	63(p+1)	84(p+1)	108(p+1)	134(p+1)

hLm beam element with 2D Legendre function

	hL2	hL3	hL4	hL5	hL6	hL7	hL8
${ND_{hLm}}^1$	8(p+1)	12(p+1)	17(p+1)	23(p+1)	30(p+1)	38(p+1)	47(p+1)
ND_{hLm}	24(p+1)	36(p+1)	51(p+1)	69(p+1)	90(p+1)	114(p+1)	141(p+1)

For hTm elements, we use polynomials defined by

$$H_{j+1}(\zeta) = [0.5(1+\zeta)]^{j+1} - 0.5(1+\zeta),\ j = 1, 2, ...$$

It is seen that for the $3D$ approximation at $p = 6$, the degree of freedom of the element is 333, while for the hierarchical element hTm ($hT6$) it is 588, and for the hierarchical element hLm ($hL6$) it is 630. Here we assumed that the polynomial degree assigned to the longitudinal approximation is 6.

Note: Given that the displacement field of the i-th element is approximated in the form $\mathbf{u}^{(i)} = \mathbf{N}^{(i)}(\xi,\eta)\psi^{(i)}(\zeta)$, the $\mathbf{N}^{(i)}(\xi,\eta)$ and $\mathbf{N}^{(i)}(\xi,\eta=\pm 1)$ matrices must be used instead of the $\mathbf{U}^{(3)}(x,y)\mathbf{R}^{(3)}_{red}$ and $\tilde{\mathbf{U}}^{(i)}(x,y^{(i)}_b)$ matrices when a Winkler-type foundation is used or the contact problem described previously has to be solved.

4. Numerical examples

4.1. Prismatic beam. Let the geometric dimensions of a prismatic beam be $a = 40$, $b = 20$, $L = 157.0796$ mm ($200\pi/4 = 50\pi$), and the material constants be: Elastic modulus $E = 2 \cdot 10^5$ MPa, Poisson's ratio $\nu = 0.3$. The beam is shown in Figure 9.

In the following we present results for two load cases. In the first load case, at the end of the rod, on the $Z = 0$ boundary, a parabolic distributed load acts in the direction y which has the resultant $F_Y = 200$ N. In the second load case a distributed load with an intensity of $p_y = -p_Y = 0.25$ N/mm^2 acts on the $y = -b/2$ surface in the direction y.

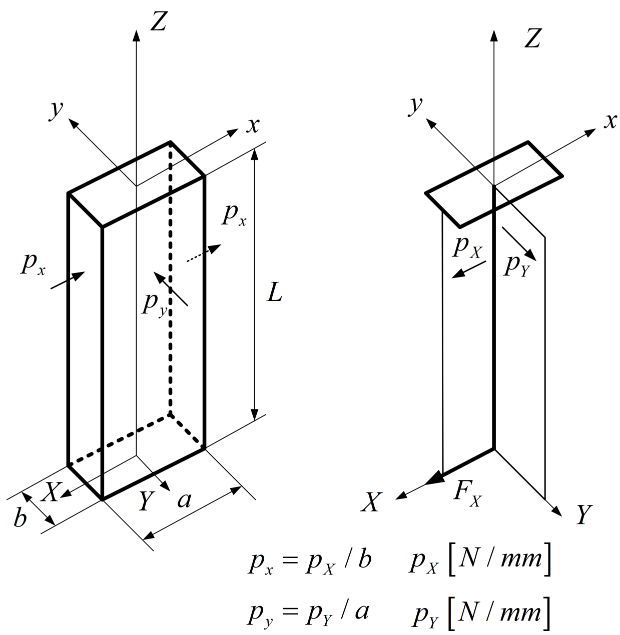

Figure 9. The geometry of a cantilever prismatic beam, the global XYZ and the local coordinate system xys ($s = Z$). The beam is fixed in the $Z = L$ plane

Solving a sequence hierarchical models, we get the results for degrees $p = 2, ..., 6$ in terms of the Y-component of the displacement of the centroid of the cross section $Z = 0$ shown in Figure 10. The results of the $3D$ finite element model (obtained by the StressCheck program) are also shown. It is clear that as the hierarchic level increases, displacement converges to the $3D$ result. The results for a sequence of hLm models are shown in Figure 11. The differences between the hierarchic models and the $3D$ finite element solution are model form errors within the family of models formulated under the assumptions of the linear theory of elasticity.

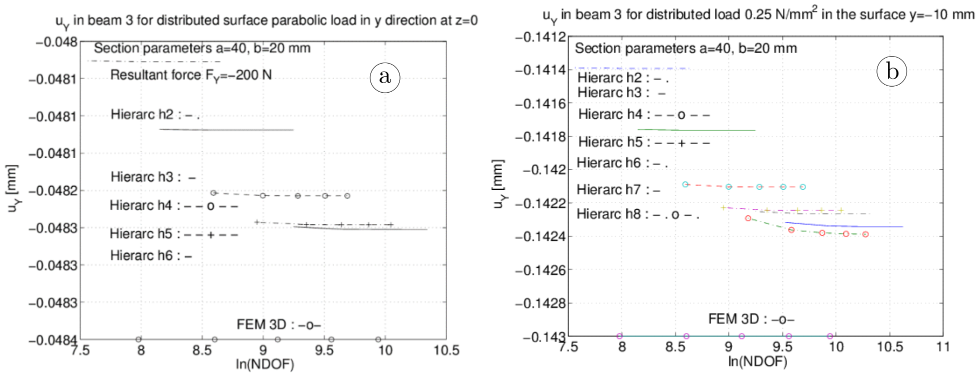

Figure 10. Convergence diagrams for hm models: a) the parabolic distributed load on the end plate acts (1st load), resulting in $F_Y = -200$ N, b) $p_y = -p_Y = 0.25\,\mathrm{N/mm}^2$ load is distributed on the $y = -b/2$ surface (2nd load)

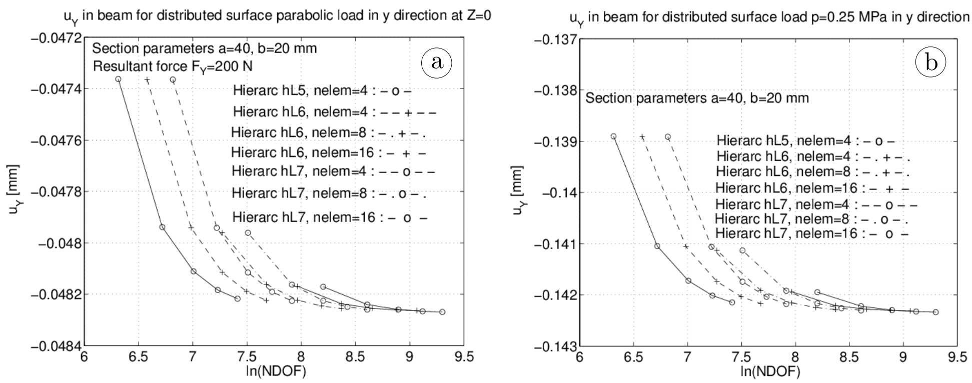

Figure 11. Convergence diagrams for hLm models, a) 1st load case, the displacement of the point $x = y = 0$ of the end plate in the Y direction in the case of different hierarchical models, b) 2nd load case

It is seen that in the case of load 2 the displacement values agree to 4 decimal digits when 16 elements and the $hL6$ and $hL7$ models are used. The numerical values are: $hL6$ – 0.482632D-01, $hL7$ – 0.482690D-01 mm for load case 1; $hL6$ – 0.142313D+00, $hL7$ – 0.142336D+00 mm for load case 2.

Solving the same problem using the Abaqus software, we get:

Mesh 1: 10 × 10 × 9.862 hexahedral elements (C3D20R), 20 nodes, quadratic, reduced integration, the number of nodes is 869 (2496 degrees of freedom, lnNDOF = 7.82) Mesh 2: 2 × 2 × 1.987 hexahedral elements (C3D20R), 20 nodes, quadratic, reduced integration, thus the total node number: 71129 (212726 unknown, lnNDOF = 12.27)

- Load case 1 for Mesh 1 -0.0541153 [mm]; for Mesh 2 -0.0485062 [mm]
- Load case 2 for Mesh 1 -0.1416740 [mm]; for Mesh 2 -0.142314 [mm].

On comparing the results with those obtained by StressCheck (load case 1 -0.0484 mm, load case 2 -0.143 mm), a much lower rate of convergence is observed.

Furthermore, we note that reduced integration introduces a type error that cannot be treated by mesh refinement. Reduced integration is one of the *variational crimes* [52].

The distributions of the stress σ_2 for the models $h3$ and $h6$ are shown for load case 2 in Figure 12. Here $p_y = 0.25$ MPa acts as a compressive stress on the surface $y = -b/2$.

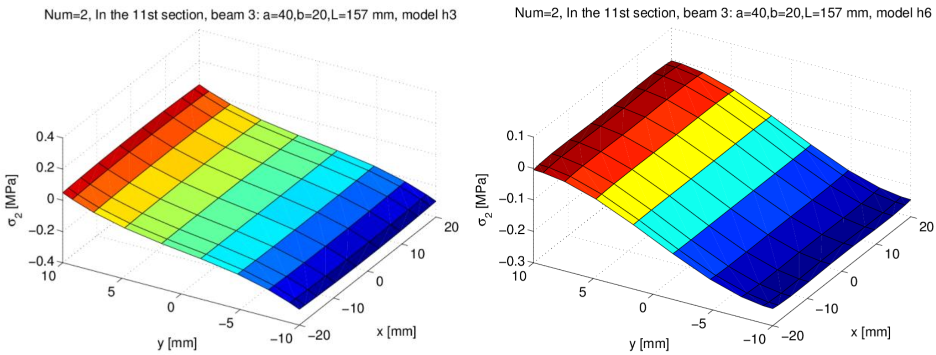

Figure 12. σ_2 stress distributions in load case 2 (models $h3$, $h6$)

We observe that the weak boundary conditions are well approximated by the $h6$ model: σ_2 is zero at the $y = 10$ mm boundary and it is $= -0.25$ MPa at the $y = -10$ mm boundary. This is not the case for lower order models such as model $h3$.

4.2. **Curved beam.** Next we consider the curved beam shown in Figure 13. The geometric parameters are: $R_0 = 100$ mm, $a = 40$ mm, $b = 20$ mm. The material is assumed to be linearly elastic, homogeneous and isotropic, the modulus of elasticity is $E = 2.0 \cdot 10^5$ MPa, Poisson's ratio is 0.3.

We examine the behavior of the structure under two load cases: In load case 1, parabolic distributed traction is applied on the cross section $\bar{\varphi} = \pi$ in the Z direction, the resultant of which is $F_z = 200$ N. In load case 2 distributed normal traction is exerted on the surface $y = -b/2$ in the Z direction, the magnitude of which is $p_y = 0.25$ MPa.

*Application of hm type elements.*The convergence diagrams obtained for two load cases are shown in Figures 14–15. The results of the $3D$ solution obtained with the StressCheck finite element program [35] are also shown. The diagrams clearly show the rapid convergence of the quantities of interest computed from the numerical solutions. The relative errors defined by

$$error = \frac{|\mathbf{u}_{FEM}| - |\mathbf{u}_{hierarc}|}{|\mathbf{u}_{FEM}|} 100\% \tag{62}$$

are below 4% for both load cases in the $h6$, $h7$ models, whereas the relative error is over 17% at the initial low hierarchical level.

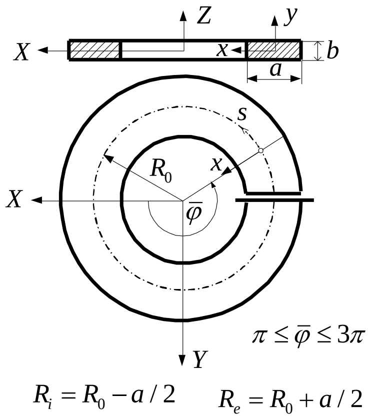

Figure 13. Geometry of the curved rod, the global XYZ coordinate system and the local xys coordinate system. The beam is fixed in the plane $\bar{\varphi} = 3\pi$

Load case 1

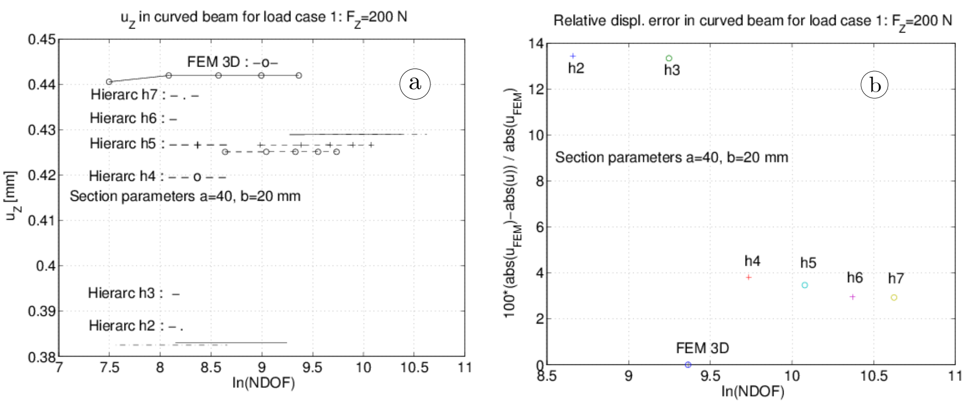

Figure 14. Convergence diagrams for hm elements for load case 1 ($F_z = 200$ N), a) displacement values, b) relative errors in displacements

Load case 2

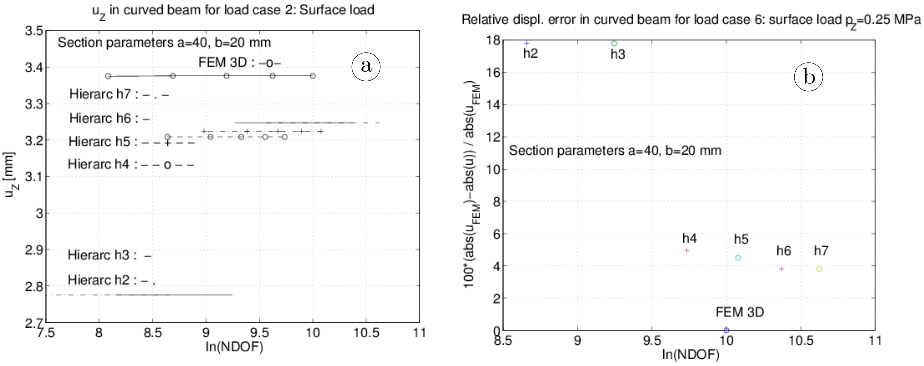

Figure 15. Convergence diagrams for hm elements in load case 2: a) displacements, b) relative errors in displacements

Application of hLm type elements. In this section we demonstrate that much faster convergence can be obtained with hLm type elements. Polynomial approximations $p = 3, 4, 5, 6$ were used in the longitudinal direction.

Load case 1:

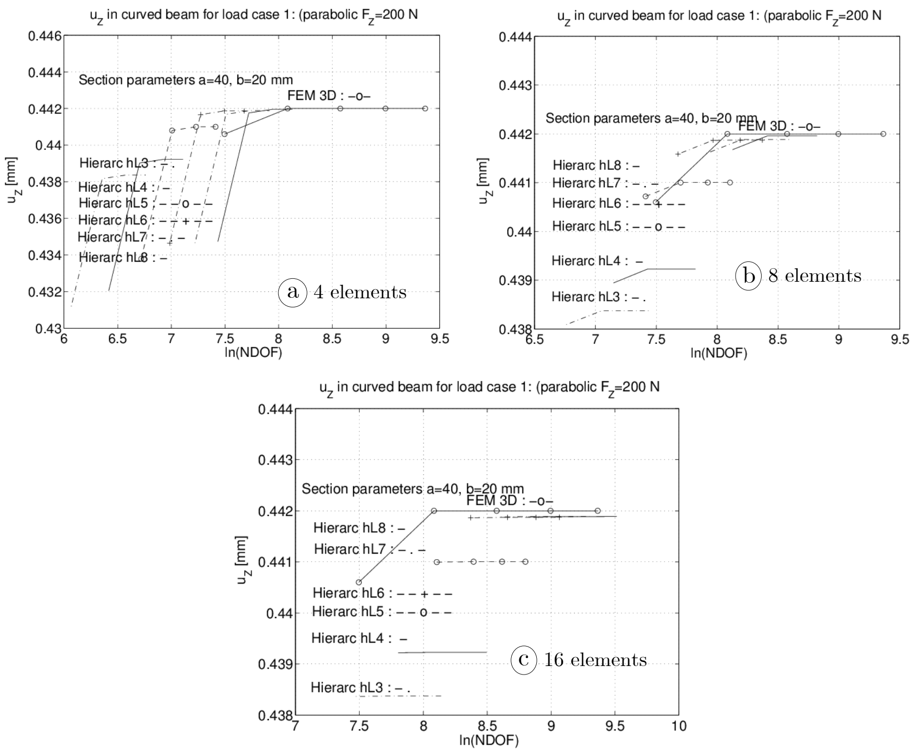

Figure 16. Convergence diagrams for hLm elements: at $F_z = 200$ N

Load case 2:

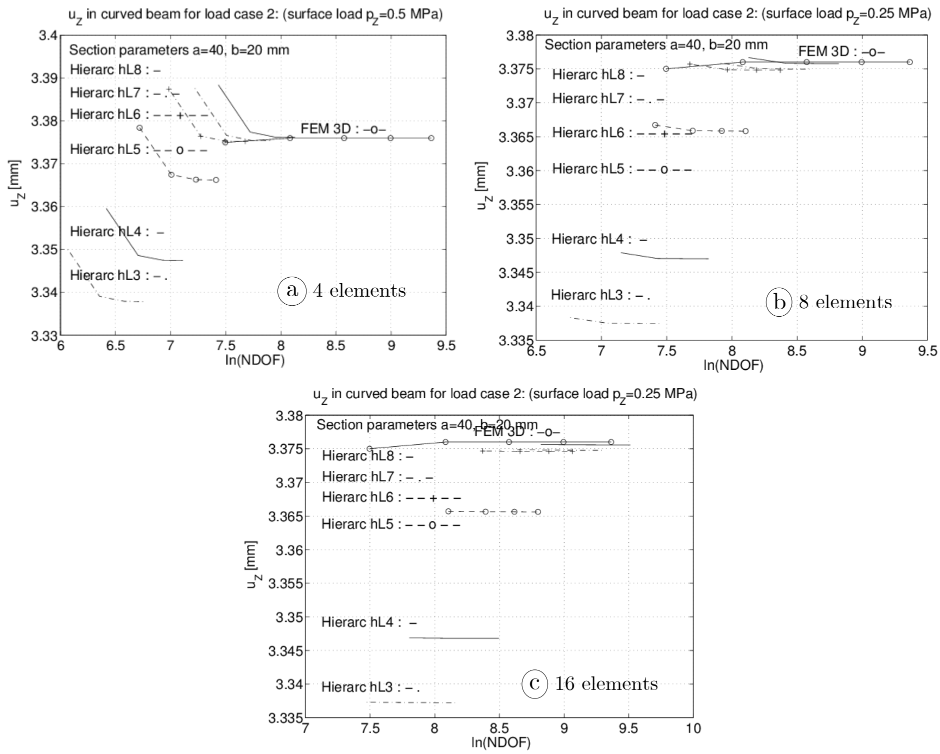

Figure 17. Convergence diagrams for load case 2

The relative errors do not exceed 1.2% when 8 elements and $p = 6 - 8$ are used.

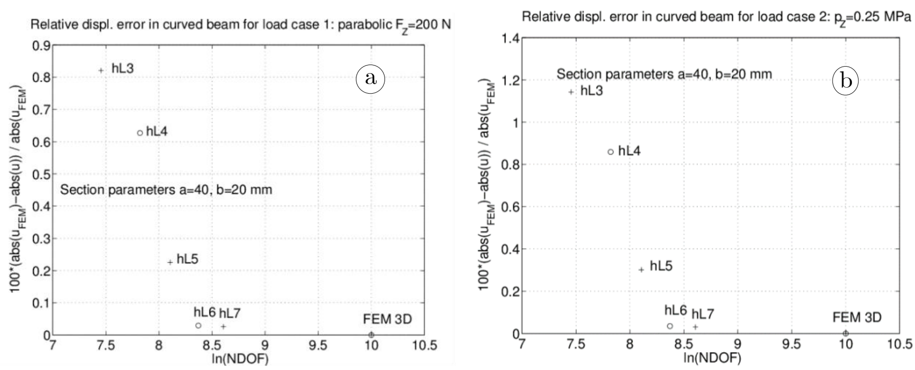

Figure 18. Relative errors for 8 elements, $p = 8$, a) in load case 1, b) in load case 2

Application of hTm elements. The relative errors in terms of the maximum displacement are shown for load cases 1 and 2 in Figure 19. Four hTm elements were used.

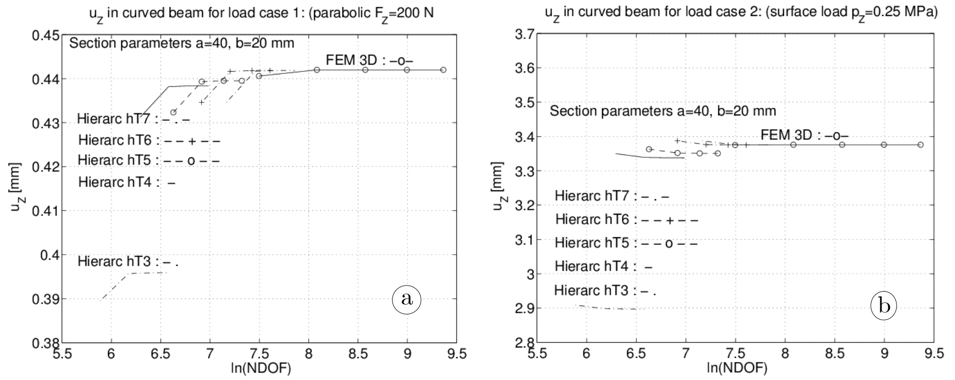

Figure 19. Convergence diagrams for load cases 1 and 2 using four htm elements

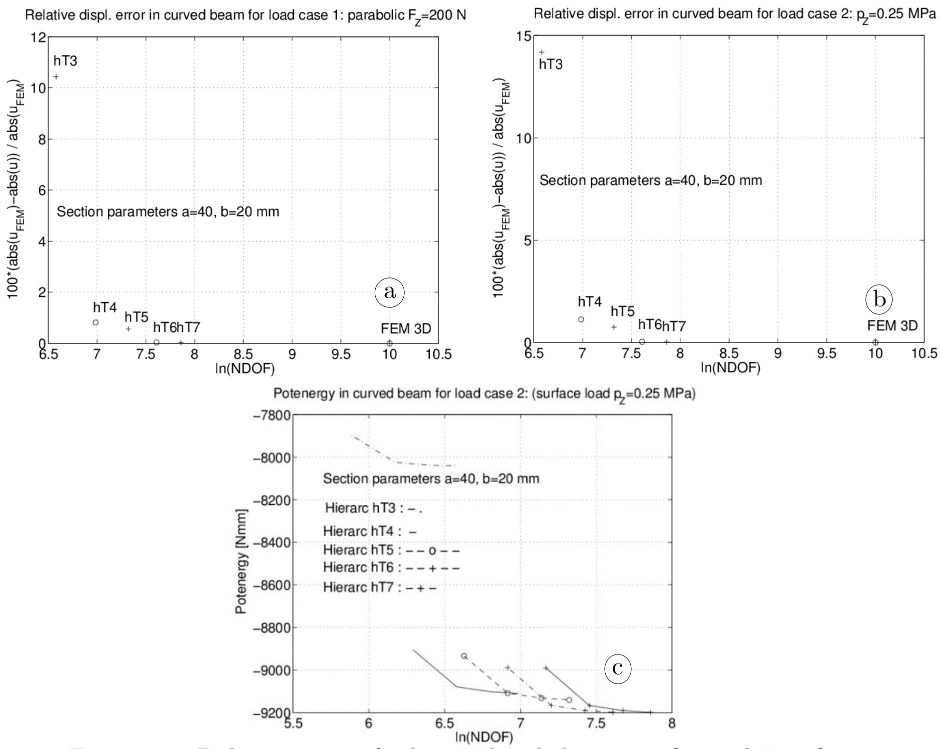

Figure 20. Relative errors for hierarchical elements of type hTm, four elements, a) load case 1, b) load case 2, c) potential energy for load case 2

Figure 20 shows the relative errors. Figure 20c shows the convergence of in potential energy. It is clearly visible that the potential energy decreases as p increases, and the smallest value was obtained by the $hT7$ model.

The hTm solution is more accurate than our original hm model. Comparing the results obtained with the hTm and hLm approximations, we can see that the hLm hierarchical approximation gives the more accurate result. This is because if the maximum degree in Taylor expansion is q, then the trunk space will have two more terms. The sum of the powers of the polynomial product terms is $q + 1$. It can be seen that the results for the excessively low $hT3$, $hL3$ hierarchical level are far from the exact solution.

4.3. **Numerical example for the contact problem of prismatic beams.** Let us consider two flexible, prismatic cantilever beams as shown in Figure 21. The geometric dimensions are: $a = b = 15$ mm. $l = 66.66$ mm. The possible contact domain is: $X \in (200, 300)$. The elastic constants are: $E^1 = 200$ GPa, $E^2 = 50$ GPa, or 20 GPa, Poisson's ratio $\nu = 0.3$. The applied load is $F_0 = 1$ kN.

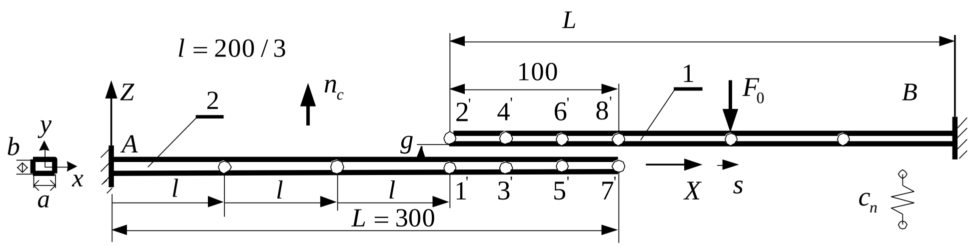

Figure 21. Contact problem of two prismatic beams. There are 12 elements. The points indicated by the open circles represent nodal points

The calculations are performed with the $h5$ hierarchical rod model.

The contact conditions are checked in the Lobatto points, see, for example, [1, 37]. The penalty parameter was set to $c_n = 1000E^1$. Moving along the X axis from right to left, we reach the point where we first find a negative d value.

At this value of X, we assume contact along the x axis in the transverse direction. We will then select this point as the penultimate integration point of the element, which we can use to determine the right-hand side, e.g. the position of the 6th node. With repeated calculations, we move the edge of the element until we reach the position in Figure 22.

Thus, there is contact on the entire surface of this element, and the one to the right already has a gap [38, 39]. Figures 22–26 show some results for this. In the case of $E^2 = 50$ GPa, nodes $3'-4'$ were moved, while in the case of $E^2 = 20$ GPa , nodes $3'-4'$ and $5' - 6'$ were moved. With the 12 element mesh, $p = 6$, the number of unknowns is $NDOF = 4464$. The contact element boundaries were established in 10–20 iterations.

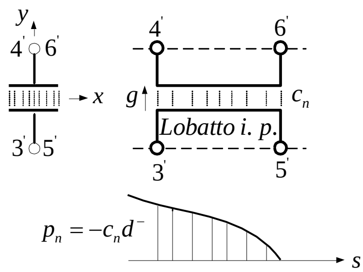

Figure 22. Contact element

Comparing the results with those calculated by the Abaqus [36] and StressCheck [35] 3D finite element programs, looking at the deflection diagrams (Figures 23, 24 and 25), we obtained very close approximations. The deformed configuration obtained with StressCheck can be seen in Figure 23b. We note that the 3D solution with $p = 6$, product space [1, 37], the number of unknowns exceeded the number of unknowns in our $h5$ hierarchical beam model by the factor of nearly 7.

The edge of the contact range and the maximum bending stress in beam 1 are as follows:

$$g = 0, \qquad X_c = 221.71 \text{ mm}, \quad \sigma^{(1)}_{\max} = 117.15 \text{ MPa},$$
$$g = 0.5, \quad X_c = 207.47 \text{ mm}, \quad \sigma^{(1)}_{\max} = 124.40 \text{ MPa}.$$

The distribution of the contact pressure as a function of s is shown in Figure 26. It is clearly visible that the solution satisfies the constraint condition $p_n d = 0$.

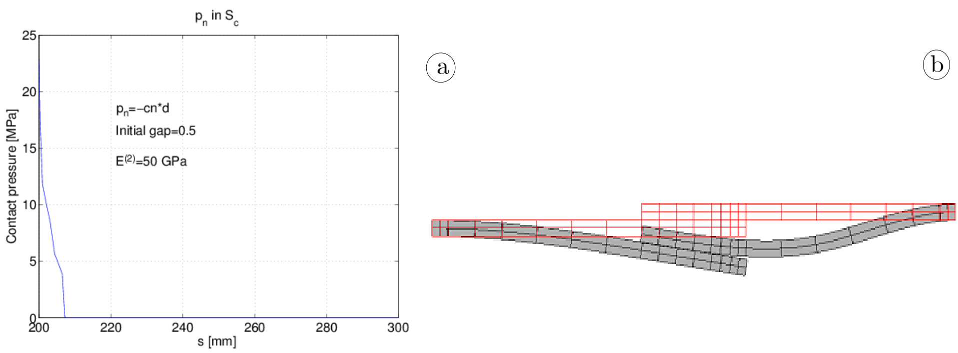

Figure 23. The modulus of elasticity of beam 2 is $E^2 = 50$ GPa, a) Contact pressure with initial gap of 0.5 mm, b) deflection obtained with the StressCheck program with zero initial gap. The number of unknowns (NDOF) is 31,104

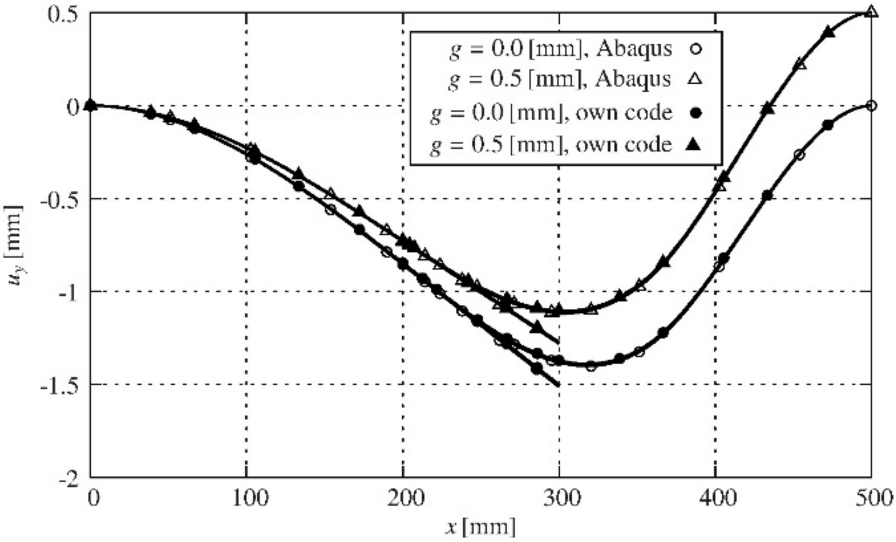

Figure 24. Deflection of the beams

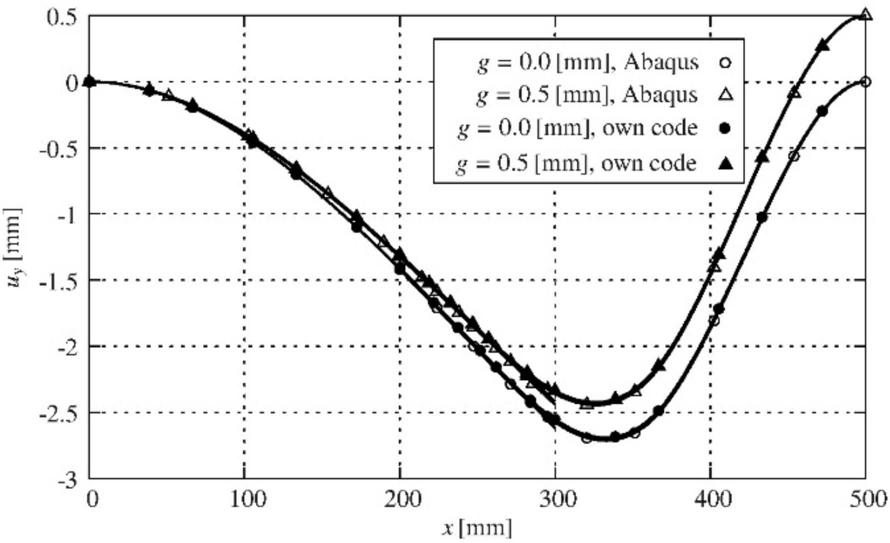

Figure 25. Deflection of the beams for beam 2 with a lower elasticity modulus ($E^2 = 20$ GPa)

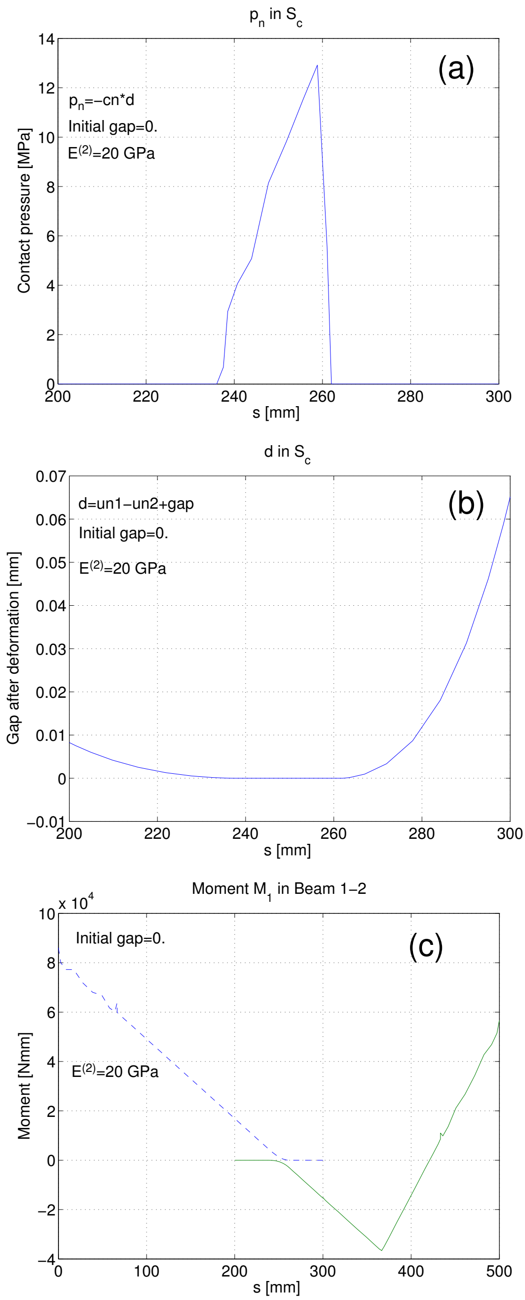

Figure 26. Modulus of elasticity of beam 2: 20.0 GPa, no initial gap: a) the contact pressure, b) the gap d after deformation, c) the resulting bending moment

The edges of the contact range and the maximum bending stress in beam 1:

$$g = 0,\ X_c = 237.52 - 262.05 \text{ mm},\ \sigma^{(1)}_{\max} = 100.71 \text{ MPa},$$
$$g = 0.5,\ \ X_c = 232.69 - 257.29 \text{ mm}\ \sigma^{(1)}_{\max} = 104.85 \text{ MPa}.$$

4.4. **Numerical example: Curved beam contact problem.** We examine the curved beam shown in Figure 13. The beam is resting on a Winkler-type elastic foundation on the surface $y = b/2$. A parabolic distributed force $F_z = 800$ N is acting on the face $\bar{\varphi} = \pi$. The geometric parameters are $R_0 = 100$ mm, $a = 40$ mm, $b = 20$ mm. The material constants are $E = 200$ GPa, $\nu = 0.3$. The Winkler constant is $c_n = 50\,\mathrm{N/mm}^2$. The beam is fixed at $\bar{\varphi} = 3\pi$. The calculations are performed using the hierarchic model $h6$, that is, the polynomial degree of the field functions is 6.

The displacement component in the Z direction on the circular curve $x = 0$, $y = -b/2$, i.e., the curve on the surface on which the Winkler boundary condition is prescribed, is shown in Figure 27. The displacement curve obtained for the Winkler support is displayed in Figure 27a. Observe that tensile stresses occur. The maximum vertical displacement estimated by our method was 0.0154 mm whereas Abaqus estimated it at 0.01616 mm, while the StressCheck estimation is 0.0164 mm. The error in our approximation, compared with StressCheck, is approximately 6%.

Assuming one-sided frictionless contact between the elastic body and the foundation, i.e. permitting compressive stresses only, the solution is shown in Figure 27b. The first element is in contact, then a gap occurs and at the end there are four elements on which contact occurs again.

The vertical displacement of the $y = b/2$ surface, corresponding to the the $h6$ model with 6 elements (NDOF = 7996), is shown in Figure 28. The convergence of the displacement of the point $x = 0$, $y = b/2$, $s = 0$ on the loaded surface and the convergence curve including the maximum occurring at $x = -a/2$, $y = b/2$, $s = 0$ of the loaded surface is shown in Table 1.

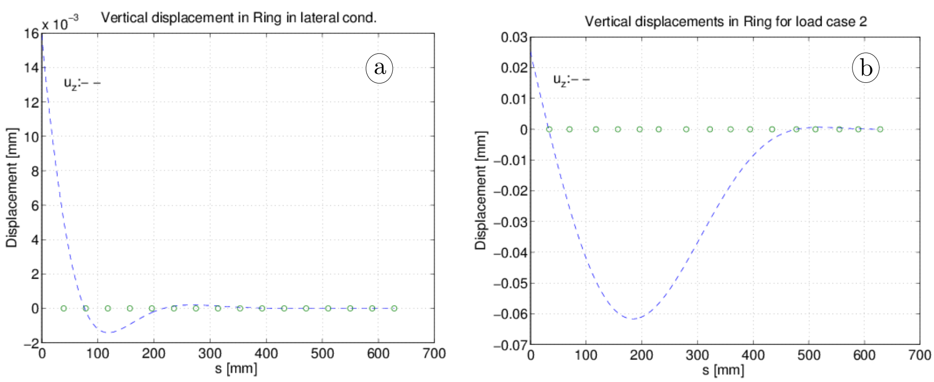

Figure 27. Displacement of the center line $x = 0$, $y = b/2$: a) Winkler support, b) contact condition

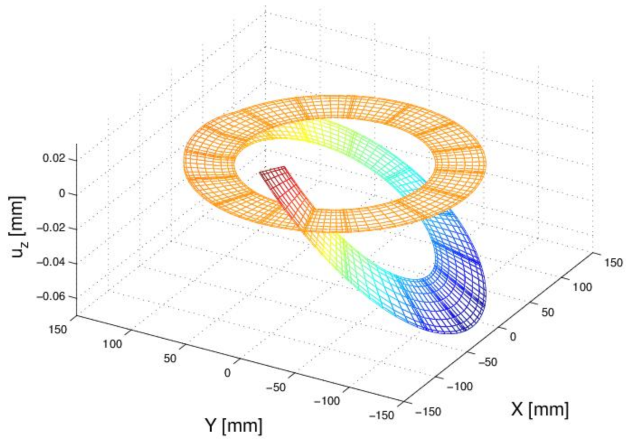

Figure 28. Vertical displacement of the surface $y = b/2$. The displacement of the point $x = 0$, $y = b/2$, $s = 0$ is equal to $\max u_z = 25.76$ μmm

Strong convergence is evident. Figure 29 shows the change in the value of the angle $\bar{\varphi}$, which marks the boundary of the first element. It can be seen that after 10 iterations we have already obtained the solution of the contact problem with negligibly small error.

Solving the problem with 3D finite element programs (Abaqus, StressCheck), we find that, considering Figures 30 and 31, the $\max u_z$ is in the point ($x = -a/2$, $y = b/2$, $s = 0$), that is $\max u_z = 29.88$ μmm obtained with Abaqus and the $\max u_z = 27.9$ μmm ($\max \sigma_z = 1.396$ MPa, $c_n = 50$ n/mm^3) obtained with StressCheck with $\max u_z = 29.61$ μmm; we used the $h6$. The calculated error is Error= $100(29.61 - 27.9)/27.9 = 6.1\%$, which is a reasonable value considering the significantly smaller number of unknowns in model $h6$. It should be mentioned that the Abaqus program is based on the h-version whereas StressCheck program is based on the p-version. The latter provides faster convergence and a sequence of solutions from which the limit value of the quantities of interest can be estimated. This is an essential requirement of solution verification.

Table 1. Demonstration of the convergence of the p-version method

p	NDF	u_z [mm] ($x = 0$, $y = b/2$, $s = 0$)	$\max u_z$ [mm] ($x = -a/2$, $y = b/2$, $s = 0$)
2	2863	0.0256558	0.02955
3	4012	0.0257587	0.02964
4	5339	0.0257623	0.02963
5	6668	0.0257666	0.02962
6	7996	0.0257685	0.02961

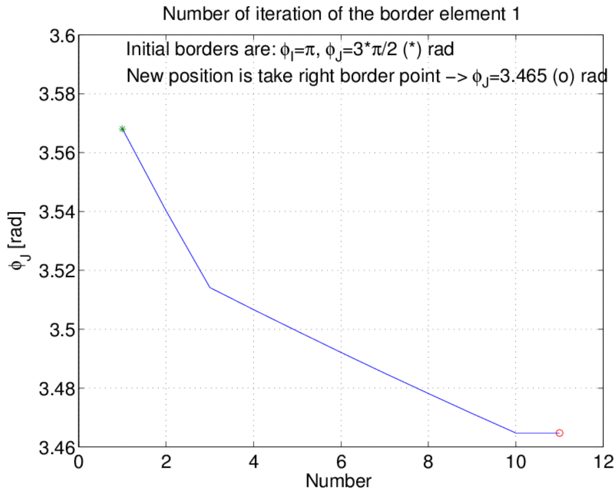

Figure 29. Location of the boundary of the first element as a function of the iteration number when the positioning technique is used

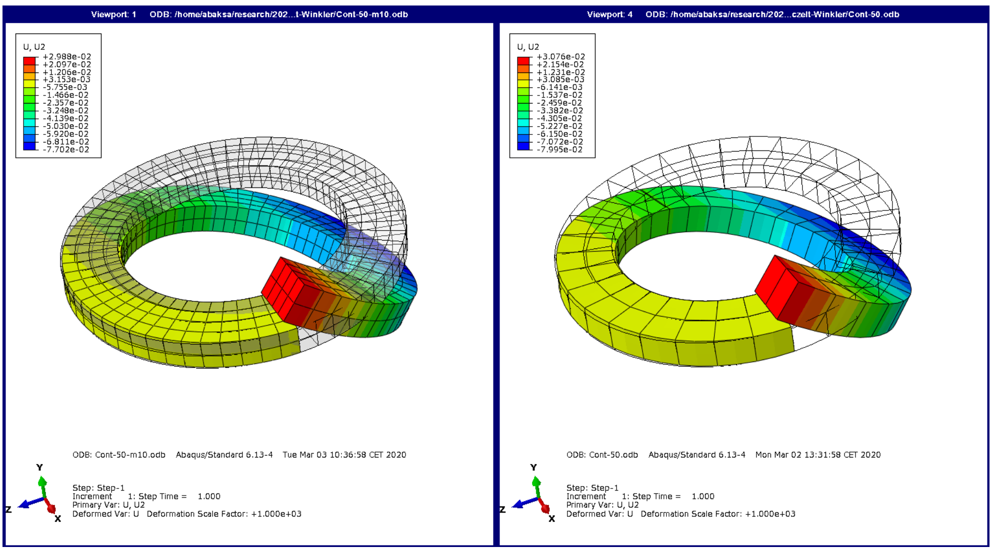

Figure 30. Solutions obtained by the Abaqus program for different numbers of elements using quadratic finite elements C3D20R (NDOF = 20343, NDOF = 6174)

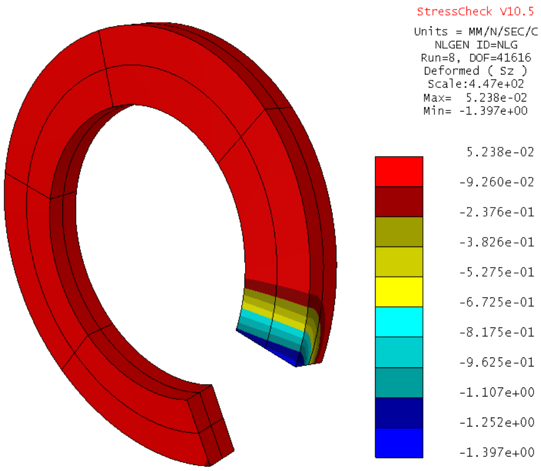

Figure 31. The distribution of σ_z obtained by the StressCheck p-version finite element program, (NDOF = 41616)

4.5. **The second numerical example for the contact problem of prismatic beams.** We examine the intersecting prismatic beams shown in Figure 32. Curved surfaces, characterized by a parabolic function, is formed on the $y = \pm b/2$ surfaces of the beams. The extent of this is characterized by the c_z amplitude value.

The elastic material parameters are Young modulus: $E = 200$ GPa, and Poisson's ratio $\nu = 0.3$. The dimensions and location coordinates of the beams result in symmetrical contact when the loads have the appropriate symmetry.

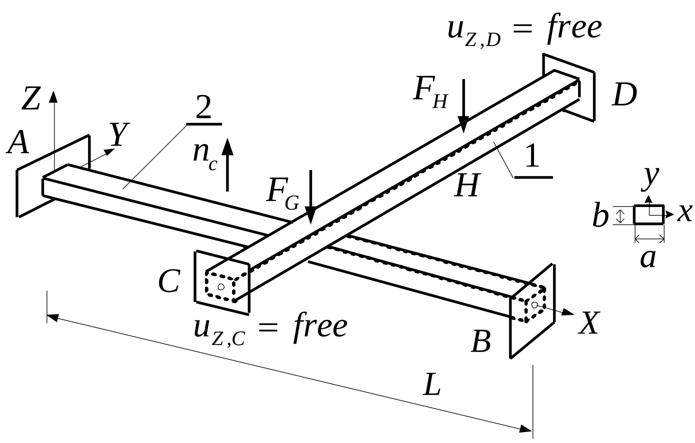

Figure 32. Configuration 2

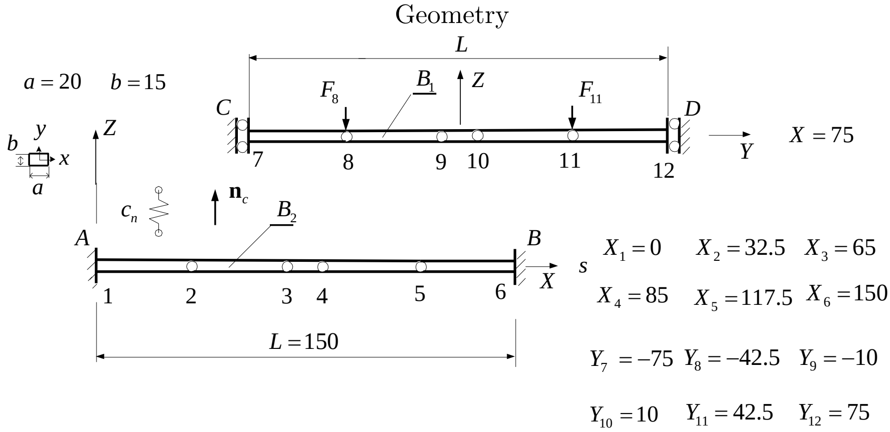

Figure 33. The dimensions of Configuration 2

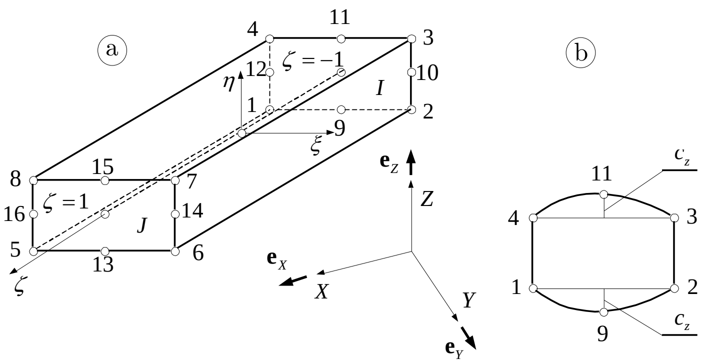

Figure 34. Finite element for mapping a) local system $-1 \leq \xi,\ \eta, \zeta \leq 1$, b) second order's boundary is characterized by parameter c_z

Load case 1:

We assign the values $F_8 = F_{11} = -F_0 = -10$ kN (in the $-Z$ direction) and fix the boundary A and B.

The $hT6$ hierarchical model and 16-node elements, shown in Figure 34, were used, however the locations of the mid-side nodes 9, 11, 13, 15 were assigned values to obtain curved surfaces. The assignment of nodes 9 and 11 is indicated in Figure 34. The assignment of nodes 13 and 15 was analogous. The penalty parameter was assigned the value $c_n = 100000$.

Using 5 elements per bar, taking into account the boundary conditions, the total number of unknowns was 4874. The forces F_8 F_{11} act as concentrated forces, since the first term of the director function in the $hT6$ model is 1. This means that the force acts in the centroid of the cross section. The initial gap is provided by the difference between the Z coordinates of the contact surfaces of bodies B_1 and B_2: $g = Z(B_1, y = -b/2) - Z(B_2, y = b/2)$. We calculate this from the finite element solution. The function obtained at $c_z = 0.1$ is a quadratic function. (See e.g. Figure 36a.)

The estimated contact pressure is shown in Figure 35. The initial gap, the displacement of the beams, the shear force and bending moment are shown in Figure 36. The contact pressure was calculated in 19×19 Gauss integration points. The contact conditions were enforced on the same 361 points. It is seen that contact occurs on a relatively small surface area which was determined by augmentation. There was no change in the final iterations, the gap between the bodies formed during the shape change: d is of the order of 10^{-3}. As expected, due to the vertical equilibrium, the resulting contact force is 10.0 kN, its line of action passes through the point $X_c = 75.0$, $Y_c = 0.0$.

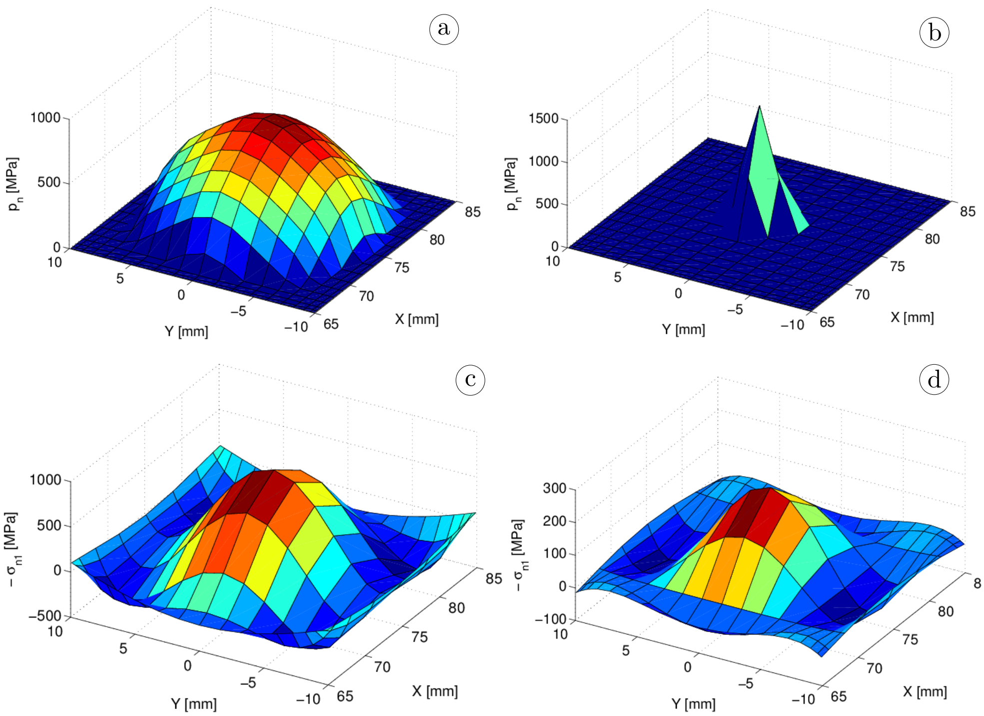

Figure 35. The distribution of the contact pressure in the configuration is shown in this figure for load case 1, a) without augmentation step = 1, b) with augmentation, step = 13, c), d) normal contact stresses calculated from Hooke's law: c) augmentation step = 0, d) augmentation step = 13

The symmetry of the displacements is clearly visible in Figure 36b. The normal stress calculated from the derivatives of the displacement field in the contact region via Hooke's law is shown in Figures 35c,d. Owing to the continuity of the approximation fields in the assumed contact region, approximated by one element, we cannot recover the negative of the contact pressure. The pressure is high in the middle of the contact domain, and small at the edges; however, the $hT6$ model cannot accurately represent the pressure distribution with the number of elements used in this example. On the other hand, the contact pressure can be reliably estimated with the augmented Lagrangian technique as indicated below.

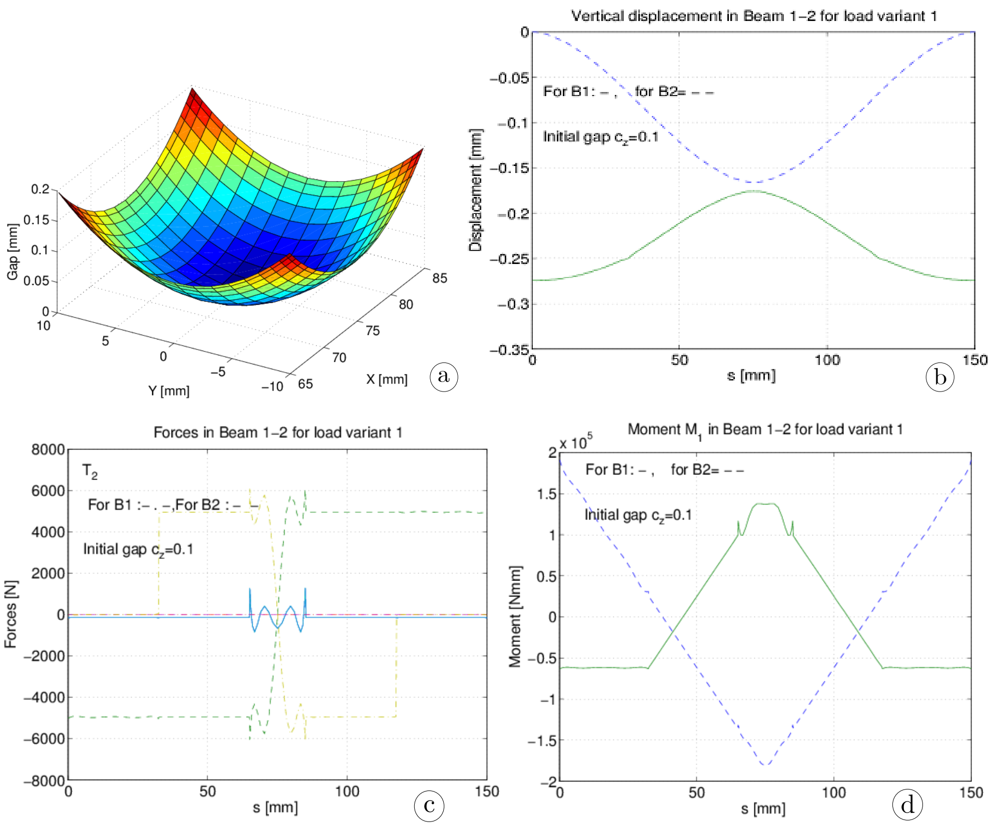

Figure 36. Results for configuration 2 at load case 1, a) initial gap function, b) vertical displacement on middle line of beam, c) distribution of the shear force T, d) bending moment M_1

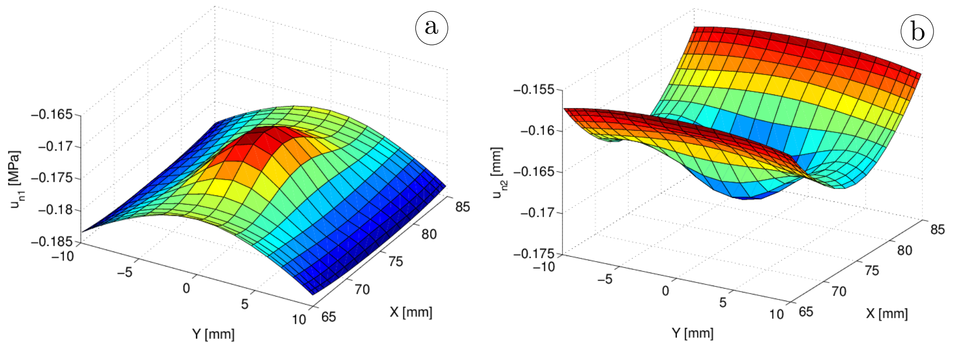

Figure 37. Vertical displacement in the contact zone, a) for body B_1, b) for body B_2 at initial gap $c_z = 0.1$, load case 1

At $c_z = 0$ the initial gap between the supports is zero. The normal stress in the corner points of the contact region is not analytic. The numerical results obtained on a grid of 19×19 Gauss points are shown in Figure 38. The resulting solution is symmetric, resulting from the contact force of $F_{cont} = 10.0$ kN.

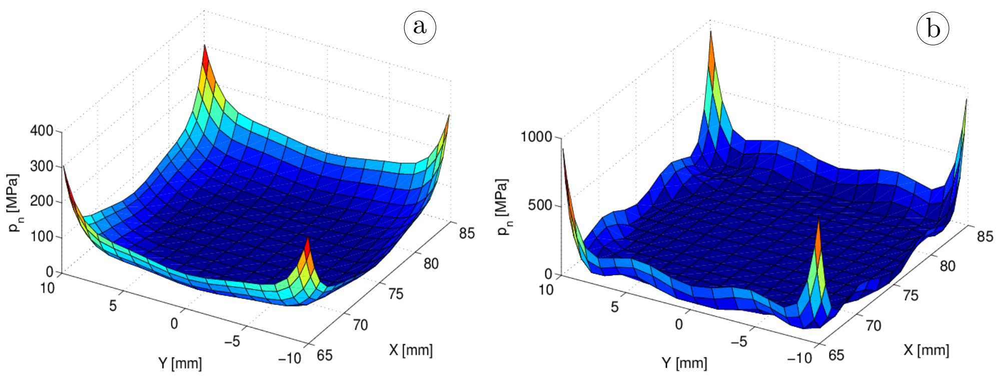

Figure 38. Contact pressure distribution interpolated on a grid of 19×19 Gauss points, a) without augmentation step $= 1$, b) with augmentation, step $= 13$. The initial gap was zero

Load case 2:
The l load is $F_c = -5$ kN (in the $-Z$ direction). Referring to Figure 32, the B and C boundaries are free, A and D are fixed.

We define second-order surfaces by letting $c_z = 0,\ 0.04,\ 0.08,\ 0.12,\ 0.4,\ 0.6,\ 0.8$. The resulting contact pressures and position of contact resulting force are shown in Table 2. Note that as the curvature decreases, the contact area shifts inward of the supposed contact area ($65 \le X \le 85$, $-10 \le Y \le 10$) and extends to a very small surface area.

At $c_z = 0$, the contact is in the left corner of the relevant domain. Then, depending on the curved surfaces of the beams, the contact shifts towards the middle of the assumed contact area.

Table 2. Resulting contact forces and their positions at different parameters c_z

c_z	X_s mm	Y_s mm	F_z kN
0.00	66.41	−9.647	6.740
0.04	67.52	−9.560	6.665
0.08	69.10	−8.596	6.474
0.12	70.68	−6.842	6.297
0.40	72.99	−2.012	6.247
0.60	74.26	−2.100	6.110
0.80	75.00	−1.500	6.049

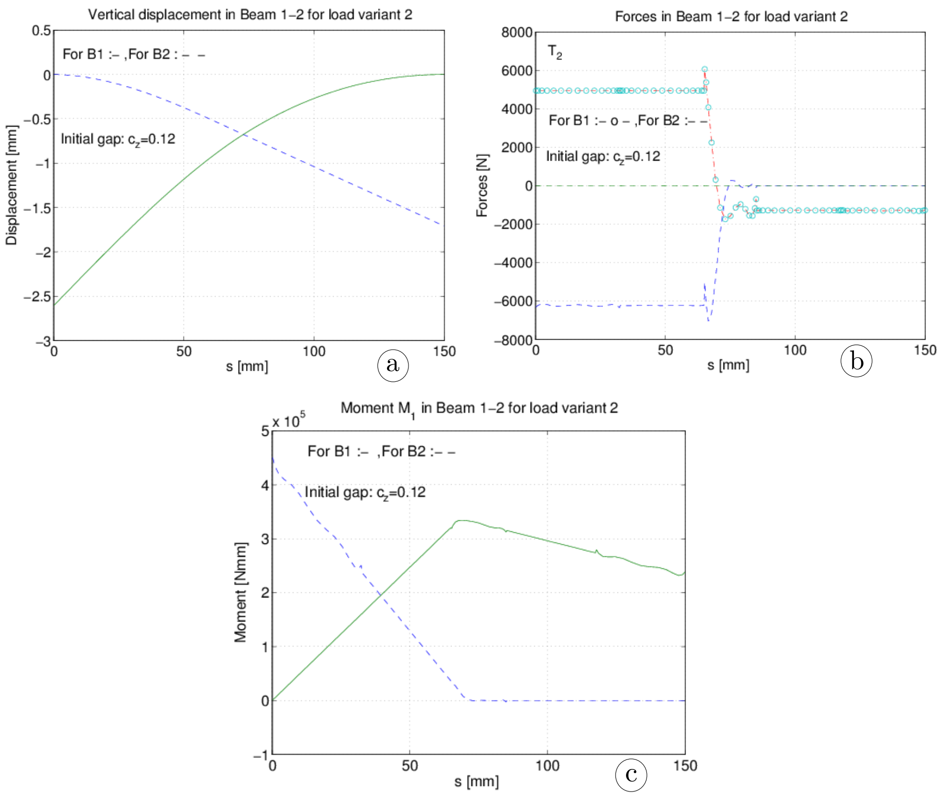

Figure 39. Results for case $c_z = 0.12$ a) vertical displacement on the center line of the beam, b) vertical displacement on middle line of beam, c) distribution of the shear force T_2, d) bending moment M_1

It is also obvious that, as the resultant of the contact pressure moves towards the larger Y by increasing $c_z = 0$, the resulting contact force decreases. The resulting distributions of bending moments and shear forces are essentially the same for different variants. Therefore only one is presented here; Figure 39 represents the case $c_z = 0.12$.

5. Summary and conclusions

We have investigated the algorithmic aspects hierarchic models for elastic rods using sequences of polynomial approximations. The models are semi-discretizations, in which the displacement components that lie in the cross-sectional plane are represented by polynomials of a fixed degree when the rod is homogeneous, or piecewise polynomials when the rod is made of composite materials. These are the director functions. The coefficients of the director functions are functions of the lengthwise coordinate and are discretized by the finite element method. In this way, the three-dimensional problem of elasticity is transformed into sets of one-dimensional problems that can be solved very efficiently. An important practical advantage is that the model form errors as well as the discretization errors can be controlled.

Classical models of rods are extensively used in conventional engineering handbooks and design manuals, see for example [53].

Through application of the algorithmic procedures outlined in this paper, is possible to extend the number and type of entries to a much broader class of problems while removing the limitations inherent in the classical formulations. In other words, numerical techniques, examples of which were discussed in this paper, allow substantial extension of the breadth and depth of the scope of classical engineering handbooks and design manuals.

Smart applications, also called 'simulation apps', are expert-designed in such a way that those applications can be used by engineers whose expertise is not in numerical simulation. The preservation and maintenance of institutional knowledge are among the important objectives of standardization. Economic benefits are realized through improved productivity and improved reliability. The challenging aspects of standardization are that (a) the input parameters have to be suitably restricted so that the assumptions incorporated in the models are not violated and (b) the model form and the discretization errors have to be controlled such that the users' expectation of accuracy, stated in terms of the quantities of interest, is satisfied. The hierarchic formulation outlined in this paper provides the algorithmic foundation for smart applications.

The hierarchical beam models can be advantageously used to solve strength problems through a model containing far fewer unknowns than fully 3D models. The complexities in implementation are compensated for by substantially shortened execution times and increased reliability.

References

1. Szabó, B. and Babuška, I. *Finite Element Analysis.* John Wiley & Sons, 1991.
2. Actis, R. L. "Hierarchic Models for Laminated Plates." PhD. Washington University in St. Louis, USA, 1991.
3. Alesadi, A., Ghazanfari, S., and Shojaee, S. "B-spline finite element approach for the analysis of thin-walled beam structures based on 1D refined theories using Carrera unified formulation." *Thin-Walled Structures,* **130**, (2018), pp. 313–320. doi: 110.1016/j.tws.2018.05.016.
4. Yan, Y., Carrera, E., Pagani, A., Kaleel, I., and de Miguel, A. G. "Isogeometric analysis of 3D straight beam-type structures by Carrera Unified Formulation." *Applied Mathematical Modelling,* **79**, (2020), pp. 768–792. doi: 10.1016/j.apm.2019.11.003.
5. Antmann, S. S. "Theory of Rods." *Handbuch der Physik.* Vol. 6/2. Springer, 1962, pp. 641–703.
6. Carrera, E. and Giunta, G. "Refined beam theories based on an unified formulation." *International Journal of Applied Mechanics,* **2**, (2010), pp. 117–143. doi: 10.1142/S1758825110000500.
7. Carrera, E., Giunta, G., Nali, P., and Petrolo, M. "Refined beam elements with arbitrary cross-section geometries." *Computers and Structures,* **88**, (2010), pp. 283–293. doi: 10.1016/j.compstruc.2009.11.002.
8. Carrera, E. and Petrolo, M. "On the Effectiveness of Higher-Order Terms in Refined Beam Theories." *Journal of Applied Mechanics,* **78**(2), (2010), 021013 (17 pages). doi: 10.1115/1.4002207.
9. Carrera, E., Giunta, G., and Petrolo, M. *Beam Structures: Classical and Advanced Theories.* Wiley-Blackwell, New York, 2011.
10. Carrera, E. and Petrolo, M. "Refined beam elements with only displacement variables and plate/shell capabilities." *Meccanica,* **47**, (2012), pp. 537–556. doi: 10.1007/s11012-011-9466-5.
11. Carrera, E., Pagani, A., and Petrolo, M. "Use of Lagrange multipliers to combine 1D variable kinematic finite elements." *Computers and Structures,* **129**, (2013), pp. 194–206. doi: 10.1016/j.compstruc.2013.07.005.
12. Carrera, E., Cinefra, M., Petrolo, M., and Zappino, E. *Finite Element Analysis of Structures through Unified Formulation.* John Wiley & Sons, London, 2014.
13. Carrera, E., Cinefra, M., Petrolo, M., and Zappino, E. "Comparisons between 1D (Beam) and 2D (Plate/Shell) Finite Elements to Analyze Thin Walled Structures." *Aerotecnica Missili & Spazio, The Journal of Aerospace Science, Technology and Systems,* **93**(3/16), (2014), pp. 1–14. doi: 10.1007/BF03404671.
14. Carrera, E., de Miguel, A. G., and Pagani, A. "Hierarchical theories of structures based on Legendre polynomial expansions with finite element applications." *International Journal of Mechanical Sciences,* **120**, (2017), pp. 286–300. doi: 10.1016/j.ijmecsci.2016.10.009.

15. De Pietro, G., de Miguel, A. G., Carrera, E., Giunta, G., Belouettar, S., and Pagani, A. "Strong and weak form solutions of curved beams via Carrera's unified formulation." *Journal Mechanics of Advanced Materials and Structures* **27**(15) (2018), pp. 1342–1353. doi: `110.1080/15376494.2018.1510066`.
16. Li, G. and Carrera, E. "On the mitigation of shear locking in laminated plates through p-version refinement." *Computers and Structures,* **225**:106121 (2019). doi: `10.1016/j.compstruc.2019.106121`.
17. Moleiro, F., Carrera, E., Zappino, E., Li, G., and Cinefra, M. "Layerwise mixed elements with node-dependent kinematics for global–local stress analysis of multilayered plates using high-order Legendre expansions." *Computer Methods in Applied Mechanics and Engineering,* **359**:112764, (2020). doi: `10.1016/j.cma.2019.112764`.
18. Szabó, B. and Sahrmann, G. J. "Hierarchic plate and shell modells based on p-extension." *International Journal for Numerical Methods in Engineering,* **27**, (1988), pp. 1855–1881. doi: `10.1002/nme.1620260812`.
19. Carrera, E., Fiordilino, G. A., Nagaraj, M., Pagani, A., and Montemurro, M. "A global/local approach based on CUF for the accurate and efficient analysis of metallic and composite structures." *Engineering Structures,* **188**, (2020), pp. 188–201. doi: `10.1016/j.engstruct.2019.03.016`.
20. Li, G., Cinefra, M., and Carrera, E. "Coupled thermo-mechanical finite element models with node-dependent kinematics for multi-layered shell structures." *Journal of Mechanical Sciences,* **171**:105379 (2020). doi: `10.1016/j.ijmecsci.2019.105379`.
21. Li, G., Carrera, E., Cinefra, M., de Miguel, A., Pagani, A., and Zappino, E. "An adaptable refinement approach for shell finite element models based on node-dependent kinematics." *Computers and Structures,* **210**, (2019), pp. 1–19. doi: `10.1016/j.compstruct.2018.10.111`.
22. Hanten, L., Giunta, G., Belouttar, S., and Salnikov, V. "Free vibration analysis of fibre-metal laminated beams via hierarchical one-dimensional models." *Hindawi Mathematical Problems in Engineering,* Article ID 2724781, 12 pages, (2018). doi: `10.1155/2018/2724781`.
23. Nguyen, D. K. and Bui, V. T. "Dynamic analysis of functionally graded timoshenko beams in thermal environment using a higher-order hierarchical beam element." *Hindawi Mathematical Problems in Engineering,* Article ID 7025750, 12 pages, (2017). doi: `10.1155/2017/7025750`.
24. Pagani, A., Carrera, E., and Ferreria A. J. M. "Higher-order theories and radial basis functions applied to free vibration analysis of thin-walled beams." *Mechanics of Advanced Materials and Structures,* **23**, (2017), pp. 1080–1091. doi: `10.1080/15376494.2015.1121555`.
25. Giunta, G., Belouettar, S., and Carrera, E. "Analysis of FGM beams by means of classical and advanced theories." *Mechanics of Advanced Materials and Structures,* **17**, (2017), pp. 622–635. doi: `10.1080/15376494.2010.518930`.

26. Giunta, G., Belouttar, S., and Frreira, A. J. M. "A static analysis of three-dimensional functionally graded beams by hierarchical modelling and collocation meshless solution method." *Acta Mechanica,* **227**, (2016), pp. 969–991. doi: 10.1007/s00707-015-1503-3.
27. Kountsawa, Y., Giunta, G., Nasser, H., and Belouttar, S. "Static analysis of shear actuated piezo-electricbeams via hierarchical one-dimensional FEM theories." *Mechanics of Advanced Materials and Structures,* **22**, (2015), pp. 3–18. doi: 10.1080/15376494.2014.907946.
28. Giunta, G., de Pietro, G., Nasser, H., Beluttar, S., Carrera, E., and Petrolo, M. "A thermal stress finite element analysis of beam structures by hierarchical modelling." *Composites B: Part B, Engineering,* **95**, (2016), pp. 179–195. doi: 10.1016/j.compositesb.2016.03.075.
29. Hui, Y., de Pietro, G., Giunta G., Belouttar, S., Hu, H., Carrera, E., and Pagani, A. "Geometrically nonlinear analysis of beam structures via hierarchical one-dimensional finite elements." *Hindawi Mathematical Problems in Engineering,* Article ID 4821385 (2018). doi: 10.1155/2018/4821385.
30. Petrolo, M., Nagaraj, M. H., Kaleel, I., and Carrera, E. "A global-local approach for the elastoplastic analysis of compact and thin-walled structures via refined models." *Computers and Structures,* **206**, (2018), pp. 54–65. doi: 10.1016/j.compstruc.2018.06.004.
31. Wu, B., Pagani, A., Filippi, M., Chen, W. Q., and Carrera, E. "Large-deflection and post-buckling analyses of isotropic rectangular plates by Carrera Unified Formulation." *International Journal of Non-Linear Mechanics,* **116**, (2019), pp. 18–31. doi: 10.1016/j.ijnonlinmec.2019.05.004.
32. Nagaraj, M. H., Kaleel, I., Carrera, E., and Petrolo, M. "Contact analysis of laminated structures including transverse shear and stretching." *European Journal of Mechanics / A Solids,* **80**,10389, (2020). doi: 10.1016/j.euromechsol.2019.103899.
33. Nagaraj, M. H., Kaleel, I., Carrera, E., and Petrolo, M. "Nonlinear analysis of compact and thin-walled metallic structures including localized plasticity under contact conditions." *Engineering Structure,* **203**, (2020). doi: 10.1016/j.engstruct.2019.109819.
34. Dauge, G. M., Faun, E., and Yosibash, Z. "Plates and Schells: Asymptotic Expansions and Hierarchic models." *Encyclopedia of Computational Mechanics,* ed. by E. Stein, R. de Borst, and T. J. R. Hughes. Vol. 1. 2004, pp. 199–236.
35. Engineering Software Research and Inc. (ESRD) Development. *StressCheck, Version 11.1.* 2023. url: https://esrd.com.
36. SIMULIA software. *ABAQUS, Version 2023.* url: https://www.3ds.com/products-services/simulia/products/abaqus/.
37. Szabó, B. and Babuška, I. *Introduction to Finite Element Analysis: Formulation, Verification and Validation.* John Wiley & Sons, 2011. doi: 10.1002/9781119993834.
38. Páczelt, I., Szabó, B., and Szabó, T. "Solution of contact problem using the *hp* version of the finite element method." *Computers & Mathematics with Applications,* **38**, (2000), pp. 49–69. doi: 10.1016/S0898-1221(99)00261-8.

39. Páczelt, I., Baksa, A., and Szabó, T. "Formulation of the p-extension finite lements for the solution of normal contact probems." *Journal of Computational and Applied Mechanics,* **15**, (2020), pp. 135–172. doi: 10.32973/jcam.2020.009.
40. Franke, D., Düster, A., Nübel, V., and Rank, E. "A comparison of the *h*-, *p*-, *hp*-, and *rp*-version of the FEM for the solution of the 2D Hertzian contact problem." *Computational Mechanics,* **45**, (2010), pp. 513–522. doi: 10.1007/s00466-009-0464-6.
41. Konyukhov, A. and Schweizerhof, K. "Incorporation of contact for high-order finite elements in covariant form." *Computer Methods in Applied Mechanics and Engineering,* **198**, (2009), pp. 1213–1223. doi: 10.1016/j.cma.2008.04.023.
42. Páczelt, I. and Szabó, T. "Solution of contact optimization problems of cylindrical bodies using the hp-FEM." *International Journal for Numerical Methods in Engineering,* **53**, (2002), pp. 123–146. doi: 10.1002/nme.395.
43. Baksa, A., Páczelt, I., and Szabó, T. "Solution of 3D contact problems using spline interpolation." *Journal of Computational and Applied Mechanics,* **9**, (2014), pp. 125–147. doi: 10.32973/jcam.2014.007.
44. Páczelt, I., Mróz, Z., and Baksa, A. "Analysis of steady wear processes for periodic sliding." *Journal of Computational and Applied Mechanics,* **10**, (2015), pp. 231–268. doi: 10.32973/jcam.2015.014.
45. Litewka, P. and Wriggers, P. "Frictional contact between 3D-beams with rectangular cross section." *Computational Mechanics,* **28**, (2002), pp. 26–39. doi: 10.1007/s004660100266.
46. Litewka, P. *Finite Element Analysis of Beam to Beam Contact.* Springer Berlin Heidelberg, 2010. doi: 10.1007/978-3-642-12940-7.
47. Kawa, O. and Litewka, P. "Contact with friction between 3d beams with deformable circular cross sections." *Engineering Transactions,* **63**, (2015), pp. 439–462.
48. Kawa, O., Litewka, P., and Studzinski, R. "Beams with deformable circular cross sections - numerical verification." *Engineering Transactions,* 66, (2018), pp. 281–299.
49. Bucalem, M. L. and Bathe K. J. *The mechanics of solids and structures - hierarchical modeling and the finite element solution.* Springer Heidelberg New York., 2011. doi: 10.1007/978-3-540-26400-2.
50. Konyukhov, A. and Schweizerhof, K. *Computational Contact Mechanics: Geometrically Exact Theory for Arbitrary Shaped Bodies.* Springer Verlag Heidelberg, 2013. doi: 10.1007/978-3-642-31531-2.
51. Wriggers, P. *Computational Contact Mechanics.* Springer Verlag Heidelberg, 2006. doi: 10.1007/978-3-540-32609-0.
52. Strang, G. and Fix, G. J. *An Analysis of the Finite Element Method.* Prentice-Hall, Inc. Englewood Cliffs, N. J., 1973.
53. Budynas, R. G. and Sadegh, A. M. *Roark's Formulas for Stress and Strain.* McGraw-Hill Education, 2020.

54. Páczelt, I. and Beleznai, R. "Nonlinear contact-theory for analysis of wire rope strand using high-order approximation in the FEM." *Computers and Structures,* **8**, (2011), pp. 1004–1025. DOI: 10.1016/j.compstruc.2011.01.011.

Appendix A. The Pascal Triangle

The Pascal triangle is the set of monomial functions shown below:

$$\begin{array}{cr}
1 & \\
x \;\; y & h1\\
x^2 \;\; xy \;\; y^2 & h2\\
x^3 \;\; x^2y \;\; xy^2 \;\; y^3 & h3\\
x^4 \;\; x^3y \;\; x^2y^2 \;\; xy^3 \;\; y^4 & h4\\
x^5 \;\; x^4y \;\; x^3y^2 \;\; x^2y^3 \;\; xy^4 \;\; y^5 & h5\\
x^6 \;\; x^5y \;\; x^4y^2 \;\; x^3y^3 \;\; x^2y^4 \;\; xy^5 \;\; y^6 & h6\\
x^7 \;\; x^6y \;\; x^5y^2 \;\; x^4y^3 \;\; x^3y^4 \;\; x^2y^5 \;\; xy^6 \;\; y^7 & h7\\
x^8 \;\; x^7y \;\; x^6y^2 \;\; x^5y^3 \;\; x^4y^4 \;\; x^3y^5 \;\; x^2y^6 \;\; xy^7 \;\; y^8 & h8
\end{array}$$

Appendix B. Mathematical transformations

In the present Appendix we detail the calculations for the terms in equation (16).

$$\mathbf{q}_I^{G,T} = \begin{bmatrix} u_{0X} & u_{0Y} & u_{0Z} & \chi_X & \chi_Y & \chi_Z \end{bmatrix}, \quad I \to J, \quad \mathbf{q}^T = \begin{bmatrix} \mathbf{q}_I^G & \mathbf{q}_J^G \end{bmatrix}^T \tag{B.1}$$

interpreted in the local system:

$$\mathbf{u}_0{}^{L,T} = \begin{bmatrix} u_{01} & u_{02} & u_{03} \end{bmatrix}, \qquad \chi^{L,T} = \begin{bmatrix} \chi_1 & \chi_2 & \chi_3 \end{bmatrix} \tag{B.2}$$

formally, the center line displacement, angular rotation and their derivatives with respect to s are approximated in the form:

$$\begin{bmatrix} \mathbf{u}_0 \\ \chi \end{bmatrix}^L = \mathbf{G}_{u\chi}\,\mathbf{q} + \mathbf{\Phi}_{u\chi,p}\,\mathbf{a}^{u\chi,p}, \qquad \begin{bmatrix} \mathbf{u}_0' \\ \chi' \end{bmatrix}^L = \mathbf{G}_{u\chi}'\,\mathbf{q} + \mathbf{\Phi}_{u\chi,p}'\,\mathbf{a}^{u\chi,p} \tag{B.3}$$

where $\mathbf{G}_{u\chi}$ is the matrix [54] linearly approximating rigid-body and elastic displacements, $\mathbf{\Phi}_{u\chi,p}$ is the matrix containing polynomials depending on the degree p, and is the vector of additional constants. The vector in equation (10), taking into account equation (B.3), can be written as

$$\tilde{\psi}_0 = \mathbf{G}^0\,\mathbf{q} + \mathbf{\Phi}_p^0\,\mathbf{a}^{0p}, \quad \mathbf{G}^0 = \begin{bmatrix} \mathbf{G}_{u\chi} \\ \mathbf{G'}_{u\chi} \end{bmatrix}, \quad \mathbf{\Phi}_p^0 = \begin{bmatrix} \mathbf{\Phi}_{u\chi,p} \\ \mathbf{\Phi'}_{u\chi,p} \end{bmatrix}. \tag{B.4}$$

By substituting equation (B.4) into equation (24), the stiffness matrix of the finite element formulation is produced [1, 37].

In some detail

$$\mathbf{\Phi}_{u\chi,p} = \begin{bmatrix} \mathbf{\Phi}_{0p} & \mathbf{0} \\ \mathbf{0} & \mathbf{\Phi}_{0p} \end{bmatrix} = \begin{bmatrix} \mathbf{\Phi}_{up} \\ \mathbf{\Phi}_{\chi p} \end{bmatrix}, \quad \mathbf{\Phi'}_{u\chi,p} = \begin{bmatrix} \mathbf{\Phi}_{0p}' & \mathbf{0} \\ \mathbf{0} & \mathbf{\Phi}_{0p}' \end{bmatrix} = \begin{bmatrix} \mathbf{\Phi}_{up}' \\ \mathbf{\Phi}_{\chi p}' \end{bmatrix} \tag{B.5}$$

Letting $\bar{s} = s/L$, where L is the length of the center line of the element, the derivative with respect to s can be calculated based on

$$(.)' = \frac{d(.)}{ds} = \frac{1}{L}\frac{d(.)}{d\bar{s}}.$$

We have

$$\underset{(3,3\times np)}{\mathbf{\Phi}_{0p}} = \begin{bmatrix} \bar{s}^2-\bar{s} & \bar{s}^3-\bar{s} & \cdots & \bar{s}^p-\bar{s} & 0 & 0 & \cdots & 0 & 0 & 0 & \cdots & 0 \\ 0 & 0 & \cdots & 0 & \bar{s}^2-\bar{s} & \bar{s}^3-\bar{s} & \cdots & \bar{s}^p-\bar{s} & 0 & 0 & \cdots & 0 \\ 0 & 0 & \cdots & 0 & 0 & 0 & \cdots & 0 & \bar{s}^2-\bar{s} & \bar{s}^3-\bar{s} & \cdots & \bar{s}^p-\bar{s} \end{bmatrix}, \tag{B.6a}$$

$$\underset{(3,3\times np)}{\mathbf{\Phi}'_{0p}} = \frac{1}{L}\begin{bmatrix} 2\bar{s}-1 & \cdots & p\bar{s}^{p-1}-1 & 0 & \cdots & 0 & 0 & \cdots & 0 \\ 0 & \cdots & 0 & 2\bar{s}-1 & \cdots & p\bar{s}^{p-1}-1 & 0 & \cdots & 0 \\ 0 & \cdots & 0 & 0 & \cdots & 0 & 2\bar{s}-1 & \cdots & p\bar{s}^{p-1}-1 \end{bmatrix} \tag{B.6b}$$

and

$$\underset{(1,6np)}{\mathbf{a}^{0p,T}} = \left[\mathbf{a}_u^{p,T}\ \mathbf{a}_\chi^{p,T}\right] \tag{B.7}$$

in which

$$\underset{(1,3\times np)}{\mathbf{a}_u^{p,T}} = \left[a_{u1}^{p=2}\ a_{u1}^{p=3}\ ,...,a_{u1}^{p}\ a_{u2}^{p=2}\ a_{u2}^{p=3},...,a_{u2}^{p}\ a_{u3}^{p=2}\ a_{u3}^{p=3},...,a_{u3}^{p}\right],$$

$$\underset{(1,3\times np)}{\mathbf{a}_\chi^{p,T}} = \left[a_{\chi 1}^{p=2}\ a_{\chi 1}^{p=3}\ ,...,a_{\chi 1}^{p}\ a_{\chi 2}^{p=2}\ a_{\chi 2}^{p=3},...,a_{\chi 2}^{p}\ a_{\chi 3}^{p=2}\ a_{\chi 3}^{p=3},...,a_{\chi 3}^{p}\right].$$

In Model-1 the matrix of strains is:

$$\boldsymbol{\varepsilon} = \begin{bmatrix} \varepsilon_1 \\ \varepsilon_2 \\ \varepsilon_3 \\ \gamma_{12} \\ \gamma_{13} \\ \gamma_{23} \end{bmatrix} = \left[\mathbf{\Gamma}_{1(0)}\ \mathbf{\Gamma}_{1(1)}\right]\begin{bmatrix} \tilde{\boldsymbol{\psi}}_0 \\ \tilde{\boldsymbol{\psi}}^{h^{(1)}} \end{bmatrix} = \mathbf{\Gamma}_1\tilde{\boldsymbol{\psi}}_1 \tag{B.8}$$

Using equations (10) and (11), the 16 functions are approximated as

$$\tilde{\boldsymbol{\psi}}_1 = \begin{bmatrix} \tilde{\boldsymbol{\psi}}_0 \\ \tilde{\boldsymbol{\psi}}^{h^{(1)1}} \end{bmatrix} = \begin{bmatrix} \tilde{\boldsymbol{\psi}}_0 \\ \mathbf{h}^{h^{(1)1}} \\ \mathbf{h}^{h^{(1)1}\prime} \end{bmatrix} = \begin{bmatrix} \mathbf{G}^0 & \mathbf{0} \\ \mathbf{0} & \mathbf{G}^{h^{(1)1}} \\ \mathbf{0} & \mathbf{G}^{h^{(1)1}\prime} \end{bmatrix}\begin{bmatrix} \mathbf{q} \\ \mathbf{q}^{h^{(1)1}} \end{bmatrix} +$$

$$+\begin{bmatrix} \mathbf{\Phi}_p^0 & \mathbf{0} \\ \mathbf{0} & \mathbf{\Phi}_p^{h^{(1)1}} \\ \mathbf{0} & \mathbf{\Phi}_p^{h^{(1)1}\prime} \end{bmatrix}\begin{bmatrix} \mathbf{a}^{0p} \\ \mathbf{a}^{h^{(1)1}p} \end{bmatrix} = \mathbf{G}_1^{total}\mathbf{q}^1 + \mathbf{\Phi}_{1p}^{total}\mathbf{a}^{1p} \tag{B.9}$$

where

$$\mathbf{G}^{h^{(1)1}} = \begin{bmatrix} 1-\bar{s} & 0 & \bar{s} & 0 \\ 0 & 1-\bar{s} & 0 & \bar{s} \end{bmatrix}, \quad \mathbf{G}^{h^{(1)1}\prime} = \frac{1}{L}\begin{bmatrix} -1 & 0 & 1 & 0 \\ 0 & -1 & 0 & 1 \end{bmatrix}, \tag{B.10}$$

$$\underset{(2,2\times np)}{\mathbf{\Phi}_p^{h^{(1)1}}} = \begin{bmatrix} \bar{s}^2-\bar{s} & \bar{s}^3-\bar{s} & \cdots & \bar{s}^p-\bar{s} & 0 & 0 & \cdots & 0 \\ 0 & 0 & \cdots & 0 & \bar{s}^2-\bar{s} & \bar{s}^3-\bar{s} & \cdots & \bar{s}^p-\bar{s} \end{bmatrix}, \tag{B.11a}$$

$$\underset{(2,2\times np)}{\mathbf{\Phi}_p^{h^{(1)1}\prime}} = \begin{bmatrix} 2\bar{s}-1 & 3\bar{s}^2-1 & \cdots & p\bar{s}^{p-1}-1 & 0 & 0 & \cdots & 0 \\ 0 & 0 & \cdots & 0 & 2\bar{s}-1 & 3\bar{s}^2-1 & \cdots & p\bar{s}^{p-1}-1 \end{bmatrix}, \tag{B.11b}$$

$$\mathbf{q}^{1T} = \left[\mathbf{q}_I^T, \mathbf{q}_J^T,\ \mathbf{q}_I^{h^{(1)1}T}, \mathbf{q}_J^{h^{(1)1}T}\right], \qquad \mathbf{q}_I^{h^{(1)1}T} = [u_{1x}\ u_{2y}]_I$$
$$I \to J \tag{B.12}$$
$$\mathbf{a}^{h^{(1)1}pT} = \left[a_{1x}^{p=2}, a_{1x}^{p=3}, ...,\ a_{1x}^{p}; a_{2y}^{p=2}, a_{2y}^{p=3}, ...,\ a_{2y}^{p}\right].$$

Based on the previous equations, it is seen that the strain vector for the *hm*-th model is:

$$\boldsymbol{\varepsilon} = \begin{bmatrix} \varepsilon_1 \\ \varepsilon_2 \\ \varepsilon_3 \\ \gamma_{12} \\ \gamma_{13} \\ \gamma_{23} \end{bmatrix} = [\boldsymbol{\Gamma}_1 \ \ \boldsymbol{\Gamma}_{h^{(2)}} \dots \boldsymbol{\Gamma}_{h^{(m-1)}} \ \boldsymbol{\Gamma}_{h^{(m)}} \ ] \begin{bmatrix} \tilde{\boldsymbol{\psi}}_1 \\ \tilde{\boldsymbol{\psi}}^{h^{(2)}} \\ \cdots \\ \tilde{\boldsymbol{\psi}}^{h^{(m-1)}} \\ \tilde{\boldsymbol{\psi}}^{h^{(m)}} \end{bmatrix} =$$

$$= \boldsymbol{\Gamma}_m \begin{bmatrix} \tilde{\boldsymbol{\psi}}_{m-1} \\ \tilde{\boldsymbol{\psi}}^{h^{(m)}} \end{bmatrix} = \boldsymbol{\Gamma}_m \tilde{\psi}_m = \mathbf{G}_m^{total} \mathbf{q}^m + \boldsymbol{\Phi}_{mp}^{total} \mathbf{a}^{mp}, \quad \text{(B.13)}$$

where

$$\tilde{\boldsymbol{\psi}}^{h^{(m)}} = \begin{bmatrix} \mathbf{h}^{(m)} \\ \mathbf{h}^{(m)\prime} \end{bmatrix} = \begin{bmatrix} \mathbf{G}^{h^{(m)}} \\ \mathbf{G}^{h^{(m)\prime}} \end{bmatrix} \mathbf{q}^{h^{(m)}} + \begin{bmatrix} \boldsymbol{\Phi} p^{h^{(m)}} \\ \boldsymbol{\Phi} p^{h^{(m)}}{}' \end{bmatrix} \mathbf{a}^{h^{(m)}p}, \quad \text{(B.14)}$$

$$\tilde{\boldsymbol{\psi}}_m = \begin{bmatrix} \tilde{\boldsymbol{\psi}}_{m-1} \\ \tilde{\boldsymbol{\psi}}^{h^{(m)}} \end{bmatrix} = \begin{bmatrix} \mathbf{G}_{m-1}^{total} & \mathbf{0} \\ \mathbf{0} & \mathbf{G}^{h^{(m)}} \\ \mathbf{0} & \mathbf{G}^{h^{(m)}}{}' \end{bmatrix} \begin{bmatrix} \mathbf{q}^{m-1} \\ \mathbf{q}^{h^{(m)}} \end{bmatrix} +$$

$$+ \begin{bmatrix} \boldsymbol{\Phi}_{mp}^{total} & \mathbf{0} \\ \mathbf{0} & \boldsymbol{\Phi}_p^{h^{(m)}} \\ \mathbf{0} & \boldsymbol{\Phi}_p^{h^{(m)\prime}} \end{bmatrix} \begin{bmatrix} \mathbf{a}^{m-1,p} \\ \mathbf{a}^{h^{(m)},p} \end{bmatrix} = \mathbf{G}_m^{total} \mathbf{q}^m + \boldsymbol{\Phi}_{mp}^{total} \mathbf{a}^{mp}, \quad \text{(B.15)}$$

$$\begin{aligned} \mathbf{G}^{h^{(m)}} &= \begin{bmatrix} \mathbf{G}_{h^{(m)}1} & \mathbf{0} & \mathbf{0} & \mathbf{G}_{h^{(m)}2} & \mathbf{0} & \mathbf{0} \\ \mathbf{0} & \mathbf{G}_{h^{(m)}1} & \mathbf{0} & \mathbf{0} & \mathbf{G}_{h^{(m)}2} & \mathbf{0} \\ \mathbf{0} & \mathbf{0} & \mathbf{G}_{h^{(m)}1} & \mathbf{0} & \mathbf{0} & \mathbf{G}_{h^{(m)}2} \end{bmatrix}, \\ \mathbf{G}^{h^{(m)\prime}} &= \begin{bmatrix} \mathbf{G}'_{h^{(m)}1} & \mathbf{0} & \mathbf{0} & \mathbf{G}'_{h^{(m)}2} & \mathbf{0} & \mathbf{0} \\ \mathbf{0} & \mathbf{G}'_{h^{(m)}1} & \mathbf{0} & \mathbf{0} & \mathbf{G}'_{h^{(m)}2} & \mathbf{0} \\ \mathbf{0} & \mathbf{0} & \mathbf{G}'_{h^{(m)}1} & \mathbf{0} & \mathbf{0} & \mathbf{G}'_{h^{(m)}2} \end{bmatrix}, \end{aligned} \quad \text{(B.16)}$$

$$\begin{aligned} \mathbf{G}_{h^{(m)}1} &= (1-\bar{s})\mathbf{E}_{(m+1,m+1)}, \quad \mathbf{G}_{h^{(m)}2} = \bar{s}\mathbf{E}_{(m+1,m+1)}, \\ \mathbf{G}'_{h^{(m)}1} &= -\frac{1}{L}\mathbf{E}_{(m+1,m+1)}, \quad \mathbf{G}'_{h^{(m)}2} = \frac{1}{L}\mathbf{E}_{(m+1,m+1)}, \end{aligned} \quad \text{(B.17)}$$

in which $\mathbf{E}_{(m+1,m+1)}$ is the unit matrix of size $(m+1, m+1)$, $\bar{s} = s/L$, $0 \le \bar{s} \le 1$. Furthermore

$$\underset{(3\times(m+1),np\times(m+1))}{\boldsymbol{\Phi}_p^{h^{(m)}}} = \begin{bmatrix} \boldsymbol{\Phi}_{h^{(m)}p} & & \\ \mathbf{0} & \boldsymbol{\Phi}_{h^{(m)}p} & \\ \mathbf{0} & \mathbf{0} & \boldsymbol{\Phi}_{h^{(m)}p} \end{bmatrix}, \quad m = 2,3,4,5,6 \quad \text{(B.18)}$$

$$\underset{(3\times(m+1),np\times(m+1))}{\boldsymbol{\Phi}_p^{h^{(m)}}{}'} = \begin{bmatrix} \boldsymbol{\Phi}'_{h^{(m)}p} & & \\ \mathbf{0} & \boldsymbol{\Phi}'_{h^{(m)}p} & \\ \mathbf{0} & \mathbf{0} & \boldsymbol{\Phi}'_{h^{(m)}p} \end{bmatrix}, \quad m = 2,3,4,5,6 \quad \text{(B.19)}$$

$$\underset{(m+1,np\times(m+1))}{\boldsymbol{\Phi}_{h^{(m)}p}} =$$

$$
= \begin{bmatrix}
\bar{s}^2-\bar{s} & \bar{s}^3-\bar{s} & \cdots & \bar{s}^p-\bar{s} & 0 & 0 & \cdots & 0 & 0 & 0 & \cdots & 0 \\
\cdots & \cdots & \cdots & \cdots & \cdots & \cdots & \cdots & \cdots & \cdots & \cdots & \cdots & \cdots \\
\cdots & \cdots & \cdots & \cdots & \cdots & \cdots & \cdots & \cdots & \cdots & \cdots & \cdots & \cdots \\
0 & 0 & \cdots & 0 & \bar{s}^2-\bar{s} & \bar{s}^3-\bar{s} & \cdots & \bar{s}^p-\bar{s} & 0 & 0 & \cdots & 0 \\
\cdots & \cdots & \cdots & \cdots & \cdots & \cdots & \cdots & \cdots & \cdots & \cdots & \cdots & \cdots \\
\cdots & \cdots & \cdots & \cdots & \cdots & \cdots & \cdots & \cdots & \cdots & \cdots & \cdots & \cdots \\
0 & 0 & \cdots & 0 & 0 & 0 & \cdots & 0 & \bar{s}^2-\bar{s} & \bar{s}^3-\bar{s} & \cdots & \bar{s}^p-\bar{s}
\end{bmatrix}
\begin{bmatrix} 1 \\ \cdots \\ \cdots \\ i \\ \cdots \\ \cdots \\ m+1 \end{bmatrix}
$$

For the sake of brevity, we provide the additional unknowns of the finite element for the $h2$ model only:

$$
\mathbf{q}^{2T} = \left[\mathbf{q}_I^{1T}, \mathbf{q}_J^{1T},\ \mathbf{q}_I^{h^{(2)}T},\ \mathbf{q}_J^{h^{(2)}T}\right] \tag{B.20}
$$

$$
\begin{gathered}
\mathbf{q}_I^{h^{(2)}T} = \left[\left[u_{1x^2}\ \ u_{2xy}\ u_{3y^2}\right]_I\ \left[u_{2x^2}\ \ u_{2xy}\ u_{2y^2}\right]_I\ \left[u_{3x^2}\ \ u_{3xy}\ u_{3y^2}\right]_I\right], \quad I \to J \\
\mathbf{a}^{h^{(2)}pT} = \left[\mathbf{a}_1^{h^{(2)}pT}, \mathbf{a}_2^{h^{(2)}pT}, \mathbf{a}_3^{h^{(2)}pT}\right], \\
\mathbf{a}_i^{h^{(2)}pT} = \left[a_{ix^2}^{p=2}, a_{ix^2}^{p=3}, ...,\ a_{ix^2}^{p}; a_{ixy}^{p=2}, a_{ixy}^{p=3}, ...,\ a_{ixy}^{p}; a_{iy^2}^{p=2}, a_{iy^2}^{p=3}, ...,\ a_{iy^2}^{p}\right],\ \ i = 1,2,3
\end{gathered} \tag{B.21}
$$

Continuing the construction of the models based on (B.15), for the $h6$ model we get:

$$
\boldsymbol{\varepsilon} = \begin{bmatrix} \varepsilon_1 \\ \varepsilon_2 \\ \varepsilon_3 \\ \gamma_{12} \\ \gamma_{13} \\ \gamma_{23} \end{bmatrix} = \left[\boldsymbol{\Gamma}_1\ \ \boldsymbol{\Gamma}_{h^{(2)}}\ \boldsymbol{\Gamma}_{h^{(3)}}\ \boldsymbol{\Gamma}_{h^{(4)}}\ \boldsymbol{\Gamma}_{h^{(5)}}\ \boldsymbol{\Gamma}_{h^{(6)}}\ \right] \begin{bmatrix} \tilde{\boldsymbol{\psi}}_1 \\ \tilde{\boldsymbol{\psi}}^{h^{(2)}} \\ \tilde{\boldsymbol{\psi}}^{h^{(3)}} \\ \tilde{\boldsymbol{\psi}}^{h^{(4)}} \\ \tilde{\boldsymbol{\psi}}^{h^{(5)}} \\ \tilde{\boldsymbol{\psi}}^{h^{(6)}} \end{bmatrix} = \boldsymbol{\Gamma}_6 \tilde{\boldsymbol{\psi}}_6 \tag{B.22}
$$

Furthermore

$$
\mathbf{G}_6^{total} = \begin{bmatrix}
\mathbf{G}^1 & 0 & 0 & 0 & 0 & 0 \\
0 & \mathbf{G}^{h^{(2)}} & 0 & 0 & 0 & 0 \\
0 & \mathbf{G}^{h^{(2)\prime}} & 0 & 0 & 0 & 0 \\
0 & 0 & \mathbf{G}^{h^{(3)}} & 0 & 0 & 0 \\
0 & 0 & \mathbf{G}^{h^{(3)\prime}} & 0 & 0 & 0 \\
0 & 0 & 0 & \mathbf{G}^{h^{(4)}} & 0 & 0 \\
0 & 0 & 0 & \mathbf{G}^{h^{(4)\prime}} & 0 & 0 \\
0 & 0 & 0 & 0 & \mathbf{G}^{h^{(5)}} & 0 \\
0 & 0 & 0 & 0 & \mathbf{G}^{h^{(5)\prime}} & 0 \\
0 & 0 & 0 & 0 & 0 & \mathbf{G}^{h^{(6)}} \\
0 & 0 & 0 & 0 & 0 & \mathbf{G}^{h^{(6)\prime}}
\end{bmatrix} \tag{B.23a}
$$

and

$$
\mathbf{\Phi}_6^{total} = \begin{bmatrix}
\mathbf{\Phi}^1 & 0 & 0 & 0 & 0 & 0 \\
0 & \mathbf{\Phi}^{h^{(2)}} & 0 & 0 & 0 & 0 \\
0 & \mathbf{\Phi}^{h^{(2)\prime}} & 0 & 0 & 0 & 0 \\
0 & 0 & \mathbf{\Phi}^{h^{(3)}} & 0 & 0 & 0 \\
0 & 0 & \mathbf{\Phi}^{h^{(3)\prime}} & 0 & 0 & 0 \\
0 & 0 & 0 & \mathbf{\Phi}^{h^{(4)}} & 0 & 0 \\
0 & 0 & 0 & \mathbf{\Phi}^{h^{(4)\prime}} & 0 & 0 \\
0 & 0 & 0 & 0 & \mathbf{\Phi}^{h^{(5)}} & 0 \\
0 & 0 & 0 & 0 & \mathbf{\Phi}^{h^{(5)\prime}} & 0 \\
0 & 0 & 0 & 0 & 0 & \mathbf{\Phi}^{h^{(6)}} \\
0 & 0 & 0 & 0 & 0 & \mathbf{\Phi}^{h^{(6)\prime}}
\end{bmatrix} \tag{B.23b}
$$

Table 3. Main characteristics of hm models

Hierarch. model	NDOF in one nodal point	Number of inner nodal points	Number of nodes for one element	AD=Additional (inner) deegre	NDOF for one element
$h1$	6	6	8	$6(p-1)$	$12+AD$
$h2$	15	15	17	$15(p-1)$	$30+AD$
$h3$	27	27	29	$27(p-1)$	$54+AD$
$h4$	42	42	44	$42(p-1)$	$84+AD$
$h5$	60	60	62	$60(p-1)$	$120+AD$
$h6$	81	81	83	$81(p-1)$	$162+AD$